Theta- and gamma-band oscillatory uncoupling in the macaque hippocampus

S. Abbaspoor[1], A.T. Hussin[2], and K.L. Hoffman[1,2]

Affiliations:

[1] Department of Psychology, Vanderbilt Vision Research Center, Vanderbilt Brain Institute, Vanderbilt University, Nashville, Tennessee

[2] Department of Biology, Center for Vision Research, York University

ABSTRACT

Nested hippocampal oscillations in the rodent give rise to temporal dynamics that may underlie learning, memory, and decision making. Although theta/gamma coupling in rodent CA1 occurs during exploration, in contrast to sharp-wave ripples that emerge in quiescence, it is less clear that these oscillatory regimes extend to primates. We, therefore, sought to identify correspondences in frequency bands, nesting, and behavioral coupling taken from the macaque hippocampus. We found that, in contrast to rodent oscillations, theta and gamma frequency bands in macaque CA1 were segregated by behavioral states. Beta2/gamma (15-70 Hz) had greater power during visual search while the theta band (3-10 Hz; peak ~8 Hz) dominated during quiescence. Moreover, theta band amplitude was strongest when beta2/slow gamma (20-35 Hz) amplitude was weakest, occurring instead concomitant with higher frequencies (60-150 Hz). Spike-field coherence was most frequently seen in these three bands, (3-10 Hz, 20-35 Hz, and 60-150 Hz); however, the theta-band coherence was largely due to spurious coupling during sharp-wave ripples. Accordingly, no intrinsic theta spiking rhythmicity was apparent. These results support a role for beta2/slow gamma modulation in CA1 during active exploration in the primate that is decoupled from theta oscillations. The apparent difference to the rodent oscillatory canon calls for a shift in focus of frequency when considering the primate hippocampus.

Introduction

Hippocampal oscillations are heralded as canonical examples of how oscillations support cognition by coordinating neural circuit dynamics (Buzsáki and Draguhn, 2004; Colgin, 2016; Hahn et al., 2019; Klausberger and Somogyi, 2008). In turn, behavioral states constrain and entrain specific neural oscillations. In rodents, locomotion and other exploratory movements elicit an ~8 Hz theta oscillation in hippocampal CA1, (Buzsáki, 2002; Kramis et al., 1975; Vanderwolf, 1969; Whishaw and Vanderwolf, 1973) and a faster gamma oscillation (25-100 Hz) that nests within theta (Bragin et al., 1995b; Colgin and Moser, 2010; Colgin, 2016; Csicsvari et al., 2003). In contrast, during quiescent states, theta and gamma oscillations are suppressed and sharp-wave ripple complexes emerge, the latter consisting of large high-frequency oscillations (150-250 Hz) in CA1 that occur within a slower (sharp-wave) deflection (Buzsáki, 2015; Ylinen et al., 1995). Although the occurrence of sharp wave ripples during quiescence is highly conserved across species (Buzsáki, 2015), its dichotomy with theta is questionable (Hussin et al., 2020; Leonard et al., 2015). This may stem from differences in how and when theta oscillations appear across phylogenetic order (Green and Arduini, 1954; Ulanovsky and Moss, 2007), particularly among primates, including humans (Courellis et al., 2019; Green and Arduini, 1954; Halgren et al., 1978; Herweg et al., 2020; Jacobs, 2014; Mao, 2022; Stewart and Fox, 1991; Talakoub et al., 2019; Tamura et al., 2013). Consequently, gamma coupling to hippocampal theta (Bragin et al., 1995a; Colgin, 2016; Lisman and Jensen, 2013), and the presence – as postulated – of sub-bands of gamma (Buzsáki and Wang, 2012; Colgin, 2016; Colgin et al., 2009; Csicsvari et al., 2003), could understandably be affected by the scarcity of theta oscillations in monkeys during species-relevant exploration (Courellis et al., 2019; Hoffman et al., 2013; Jutras et al., 2013; Leonard et al., 2015; Mao et al., 2021; Skaggs et al., 2007; Talakoub et al., 2019). In the present study, we, therefore, adopted a hypothesis-generating (data-driven) approach to identify i. which oscillatory bands emerge in macaque hippocampal CA1 as a function of the behavioral state; ii. whether these oscillations coalesce or compete, and iii. to what extent local single units are modulated at these rhythms.

Results

Spectral analysis of hippocampal LFP during active visual search and quiescence

We recorded 42 sessions (M1: 26 sessions, M2: 16 sessions) in the hippocampal CA1 subfield of two macaques (Figure 1; Figure 1- figure supplement 1) during active visual search and quiescence (henceforth: 'rest'). As a control for the effects of the stationary animal, we recorded from one of the above animals (M2) and a third animal (M3) in freely moving and overnight sleep conditions (Figure 1 – figure supplement 2). Consistent with previous reports

(Leonard and Hoffman, 2017; Leonard et al., 2015), we observed bouts of roughly 20-30 Hz oscillations predominantly during search, and slower-frequency, larger-amplitude local field potentials (LFPs) during rest (Figure 1A, C). To visualize the relationship between spectral power across frequency bands, we sorted quantiles of ~1 s segments based on their average power in the 20-30 Hz frequency band, revealing an antagonistic relationship between 20-30 Hz and <10 Hz frequencies (Figure 1B) i.e. when power at 20-30 Hz was greatest, <10 Hz power was qualitatively weakest. In contrast, stronger power at <10 Hz was accompanied by stronger power at > 80 Hz. To determine whether the spectrum varies with behavioral epoch, as it does in rodents (Buzsáki, 1996; Whishaw and Vanderwolf, 1973), we calculated the power spectrum for each behavioral state (Figure. 1D). To identify power beyond the 1/f background, we used the aperiodic-adjusted power spectrum (Demanuele et al., 2007; Donoghue et al., 2020). We found stronger 7-10 Hz power during rest compared to active search (Figure. 1D, Middle). In contrast, power in the higher frequencies from 15-70 Hz was stronger during active search compared to rest, with a peak in the 20-30 Hz range (both, $p<0.05$ Wilcoxon signed rank test with FDR correction). In most non-rodent species examined, including humans, hippocampal theta band oscillations during alert wakefulness are described as occurring intermittently, in short-lived bouts, unlike the protracted and predictable trains of theta oscillations seen in the rodent hippocampus (Green and Arduini, 1954; Jacobs, 2014; Jutras et al., 2013; M Aghajan et al., 2017; Talakoub et al., 2019; Ulanovsky and Moss, 2007; Watrous et al., 2013). To identify oscillations that are rare and short-lived, and to allow for a more direct comparison to conventions used in human iEEG/macroelectrode studies, we used the BOSC method (Caplan et al., 2001; Hughes et al., 2012; M Aghajan et al., 2017). This method quantifies the fraction of time that band-limited power exceeds amplitude and duration thresholds. The amplitude threshold is set after fitting the signal to a log-log linear regression to account for the spectral tilt ($1/f^x$) of the distribution under consideration and accepting only residuals with at least 3 cycles exceeding 95% of the χ^2 distribution. This classifies the graded power spectral measure into discrete 'hits' and 'misses' across time. Consistent with continuous power spectral results, we found that theta bouts ('hits') were more prevalent during rest/sleep compared to online active behavioral states. The pattern was the opposite for beta2/gamma frequencies, which were more prevalent during active states (Figure 1-figure supplement 2, $p<0.05$ Wilcoxon signed rank test with FDR correction).

In rodents, the frequency and the amplitude of theta oscillation are related to the speed of locomotion (Buzsáki, 2002; Fuhrmann et al., 2015; McFarland et al., 1975; Sheremet et al., 2016) although theta activity is also observed during awake immobile states of alertness (Kramis et al., 1975; Sainsbury, 1998; Tai et al., 2012; Vanderwolf, 1969). Theta-movement correlates raise the concern that the scarcity of theta during active behaviors in the present

study might be attributed to the animals' immobility. To address this concern, we recorded wirelessly from the hippocampal CA1 of the second monkey (M2) and a third adult female macaque (M3) during freely-moving active states including immersive visual search and during overnight rest/sleep (M3: 15 sessions, M2: 3 sessions). The results match those of the previous experiment, thereby demonstrating that the decrease in theta-band power and the increase in gamma power during active behaviors generalize, i.e. they were not merely due to the immobile state of the animals (Figure 1-figure supplement 3, Video 1). Furthermore, the duration and consistency of theta bouts during early sleep indicate that these methods (recording sites, electrode signal, and states) are capable of detecting theta oscillations, but that they appear during different epochs than those for recordings in rats and mice, (Figure 1-figure supplement 3, Video 1, Figure 1-figure Supplement 4).

Hippocampal cross-frequency coupling

To assess the coupling of theta and gamma oscillations at a finer temporal scale, we computed the cross-frequency power correlations across the spectrum. Consistent with the qualitative pattern shown in Figure 1B, power at 3-8 Hz and 20-35 Hz were negatively correlated (Fig. 1E, $p<0.05$, using a cluster-based permutation test corrected for multiple comparisons). In addition, power in the slower, 3-8 Hz band was positively correlated with that of a much faster, 80-150 Hz band. We next applied a complementary approach, comparing the amplitude envelopes of these two bands (theta and slow gamma) over time, to track the finer temporal structure of power correlations. The results supported the epoched-data results (Figure 1-figure supplement 2).

To estimate phase-amplitude coupling in the LFP, we performed bicoherence analysis, (Figure 1F; (Giehl et al., 2021; Hyafil, 2015; Kovach et al., 2018), revealing a peak cluster around the 25 Hz frequency range which confirms an interaction between the activity at this frequency and its second harmonic. In addition, the 3-8 Hz band was coupled to high frequencies of 95-150 Hz ($p<0.05$, cluster-based Monte Carlo statistical test). This is consistent with our cross-frequency amplitude coupling results and indicates that the correlated envelopes in Fig. 1E are driven by the phase-specific coupling of the high frequencies (Figure 1B). However, our bicoherence results showed no significant phase-amplitude coupling between theta and gamma frequency ranges.

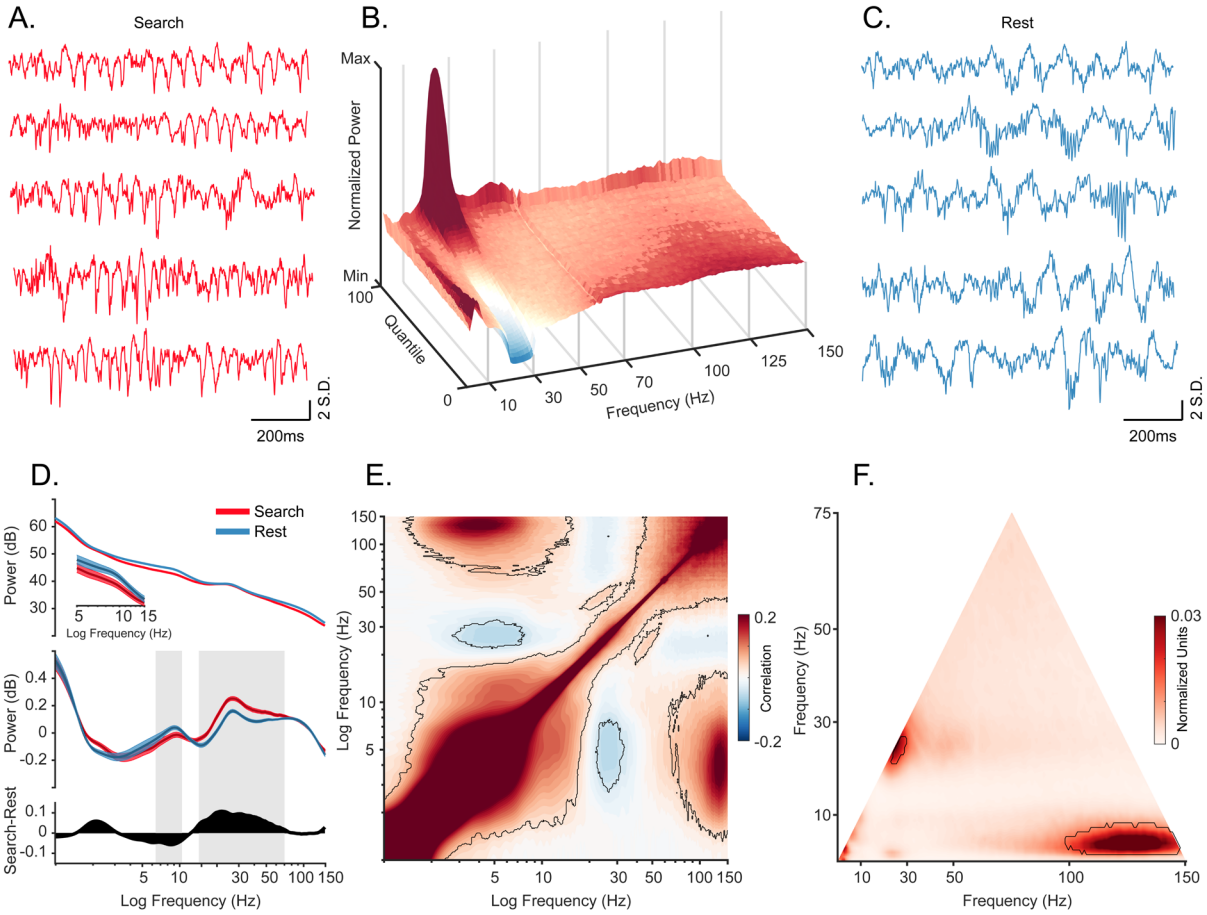

Figure 1. Oscillatory decoupling in CA1 field potentials. A. Example traces of broadband LFP in CA1 during search. Data segments were taken from epochs with characteristic high 20-30 Hz power, shown in B (traces were linearly detrended for visualization). **B.** Spectral density sorted by 20-30 Hz power. The surface plot shows data segments sorted into quantiles according to 20-30 Hz power, revealing an apparent increase in 5-10 Hz power when 20-30 Hz power is weakest. See Methods for details. **C.** Example traces of wideband LFP in CA1 during the rest epoch showing characteristic interactions between <10 Hz and >60 Hz oscillations. Conventions as in A. **D.** ***Top.*** Mean power spectral density during search (red), and rest (blue). *Inset*: mean power for low frequencies of the main plot, with shaded 95% bootstrap confidence interval (N=42 sessions). ***Middle.*** Power spectral density after fitting and subtracting the aperiodic 1/f component during search and rest, with shaded 95% bootstrap confidence intervals. Gray areas show significant differences in power across behavioral epochs ($p<0.05$, Wilcoxon signed rank test, FDR corrected) ***Bottom.*** Power difference between search and rest. **E.** Average cross-frequency power comodulogram (N=42 sessions). Dark outline represents areas that were significant in at least 80% of samples ($p < 0.05$, cluster-based permutation test corrected for multiple comparisons). **F.** Average bicoherence of the CA1 LFP (N=42 sessions). The dark outline represents areas that were significant in at least 80% of sessions ($p < 0.05$, Monte Carlo test corrected for multiple comparisons). The decoupling is preserved when applying analysis methods sensitive to transient oscillations (Figure 1-figure supplement 2), and when analyzing CA1 LFPs from an additional monkey who moved freely in a search task, and during night-time rest (Figure 1-figure supplement 3).

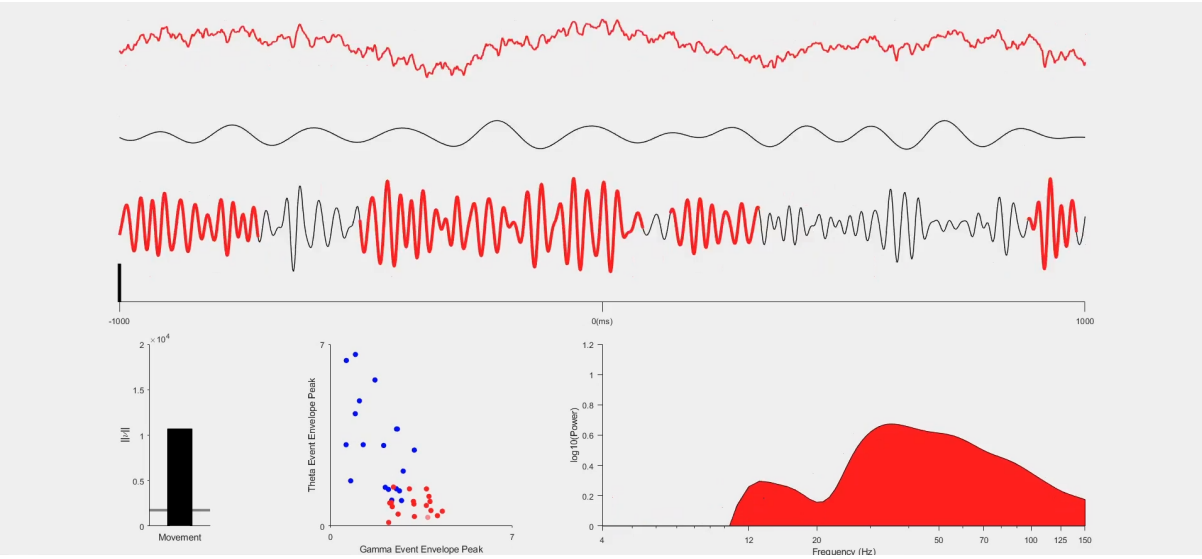

Video 1. Oscillatory dynamics in monkey CA1 during sleep and waking states *(Top)* Broadband LFP during sleep (blue), and free movement in an enclosure during a search task (red), the 4-8 Hz bandpass filtered LFP, and the 25-50 Hz LFP, shown top to bottom, respectively. Detected bouts in each frequency band are highlighted with blue (sleep) and red (waking). The black vertical line shows 3 S.D. above the mean. ***(Bottom)*** **Left**: Movement, expressed as the vector norm of angular velocity. The grey horizontal line shows the threshold for movement. **Middle**: The envelope peak of detected theta (4-8 Hz) bouts plotted as a function of the gamma (25-50 Hz) peaks. **Right**: 1/f corrected (fitted residual) power spectrum. The distribution of power shifts to higher frequencies during awake compared to sleep.

Oscillatory modulation of spiking activity

Peaks in spectral power do not necessarily indicate the presence of oscillations in the underlying neural activity (Buzsáki and Wang 2012; Pesaran et al. 2018; Herweg et al. 2020; Jones 2016). If oscillations are present in the local neural population, regular comodulation between spikes and local field oscillation phases should occur. We measured the spike-field coherence for the whole duration of the sessions by calculating pairwise phase consistency (Vinck et al., 2010) for well-isolated units (N=404). Individual cells phase locked to multiple frequencies (Figure 2A; $p<0.05$, permutation test and Rayleigh test $p<0.05$), with the population showing the full range of spike preferred frequencies of modulation (Figure 2C).

One of the caveats of spike-field coherence measures is that they can be sensitive to large amplitude non-periodic deflections. Sharp-wave ripples (SWRs) have a non-oscillatory amplitude envelope within the frequency range of 0.1 to 10Hz in rodents and non-human primates (Hussin et al., 2020; Leonard et al., 2015; Maier et al., 2003; Rex et al., 2009; Skaggs et al., 2007). Furthermore, we previously observed that SWRs occur in primates during active visual exploration (Leonard and Hoffman, 2017; Leonard et al., 2015) and that the probability of firing of cells increases during these events, for putative pyramidal and inhibitory cells alike (Hussin et al., 2020; Leonard et al., 2015; Skaggs et al., 2007). Given the

limitations of spike-field coherence, the frequency characteristics of SWRs, spiking activity profile of neurons around these events, weaker power at 7-10 Hz during active search, and the strong coupling between bands matching the SWR events (3-8 Hz and >95 Hz), we hypothesized that spike-LFP coherence at low frequencies might be partly produced as a byproduct of the slow deflection of sharp-wave ripples (Hussin et al., 2020) rather than via harmonic oscillations. To test this, we extracted peri-SWR spikes, computed PPC only for these spikes in each cell [PPC_{swr}], and then compared this to the PPC for spikes outside the SWR windows [$PPC_{residual}$]. Figure 2B shows an example cell that exhibits stronger spike-LFP coherence at 8 Hz during SWR than outside the SWR window ($p<0.05$, permutation test with FDR correction). At the population level, coherence at lower frequencies (2-10 Hz) was greater during SWR than in the SWR-removed distributions. In contrast, the higher frequencies (10-200Hz) maintained a greater coherence outside of the SWR time window (Figure 2D). This led to weaker mean spike-field coherence restricted to the < 10 Hz range, after removing the influence of SWRs, suggesting a contribution of the non-oscillatory slow deflections in the SWR complex to the apparent cross-frequency interactions.

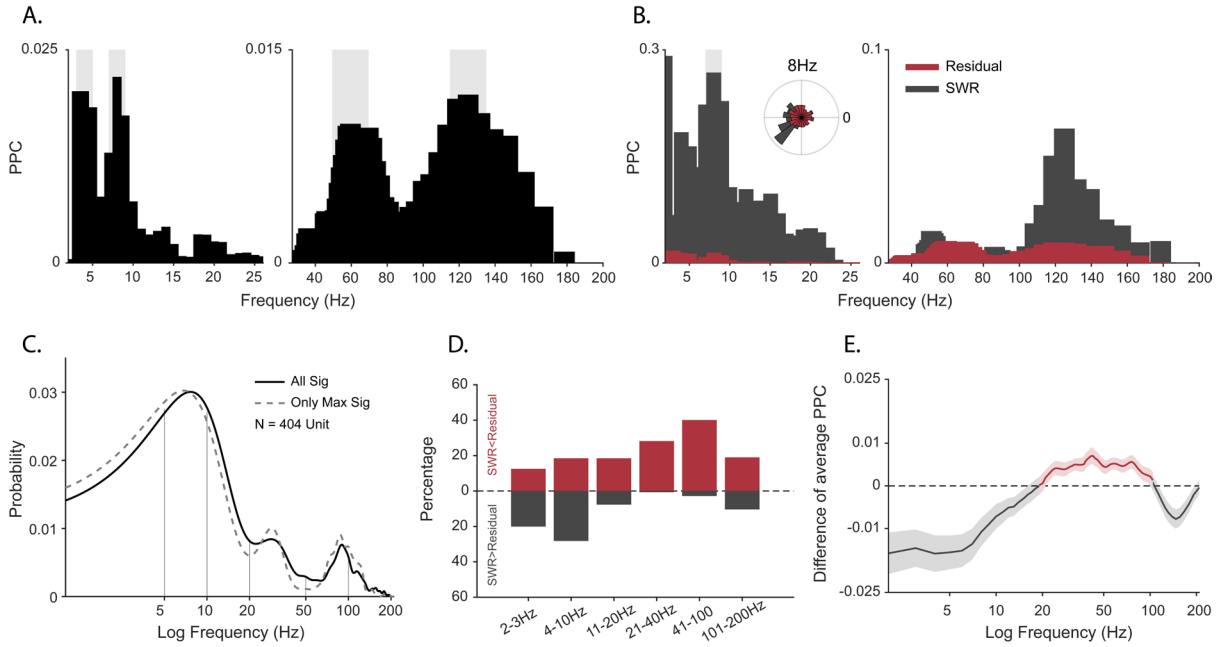

Figure 2. Spike-field coherence and its influence by sharp-wave ripples. A. Spike-LFP Pairwise phase consistency (PPC) spectra for an example unit. Shaded gray shows significant values ($p<0.05$, permutation test, and Rayleigh test $p<0.05$). **B.** Spike-LFP coherence for spikes during detected SWRs (dark gray) and for spikes remaining after extracting the SWR epochs ('residual', red). Light gray shading shows a significant difference at $p < 0.05$ in the FDR-corrected permutation test for the SWR group. Inset: Normalized histogram of the phase values at 8 Hz, obtained from the spike-LFP coherence analysis shown in A. **C.** Probability distribution of observing significant PPC values across all frequencies (solid black line), and only for preferred frequency (frequency with maximum PPC value) before adjusting for SWRs (N = 404 units). **D.** Difference in the proportion of cells with greater spike-LFP coherence for SWR (grey) and SWR-removed residual (red), for 6 frequency bands (N=185 units).

E. SWR-residual difference of mean Spike-LFP coherence. Shading shows 95% bootstrapped confidence interval. Positive values indicating greater PPC for residual than SWR groups are shown in red, negative values (SWR>residual) in dark gray.

To ensure that oscillations were local and to avoid the influence of aperiodic deflections, we generated spike autocorrelograms. Periodic peaks of the spike autocorrelograms demonstrate theta rhythmicity in rat and mouse CA1 (Cacucci et al., 2004; O'Keefe and Recce, 1993; Royer et al., 2010). To directly compare theta rhythmicity in our cell population with observations in the rodent, we computed the autocorrelogram for a complete population of well-isolated cells with at least 100 spikes for the whole session and for the complete cell population from homologous subregions of CA1 in rodents, also across the whole session. Figure 3A shows an autocorrelogram of the theta spike-field coupled cell in Figure 2A (black, monkey) overlaid onto a theta-rhythmic cell from the homologous CA1 region of a rat (i.e. temporal CA1) shown in gray. To quantify theta autocorrelogram rhythmicity, we calculated the theta modulation index (52). Compared to modulations seen in the rat (Figure 3B in gray), monkey cells typically showed near zero index values i.e. were not modulated (Figure 3B in black), which was also evident in the sorted-cell and mean population autocorrelogram (Figure 3C, inset shows rat distribution). For a given firing rate, higher frequencies are less likely to demonstrate cycle-by-cycle periodicity due to their shorter periods; nevertheless, we observed a few examples of >20 Hz spike modulation in the spike-triggered averages and autocorrelograms of several cells (Figure 4).

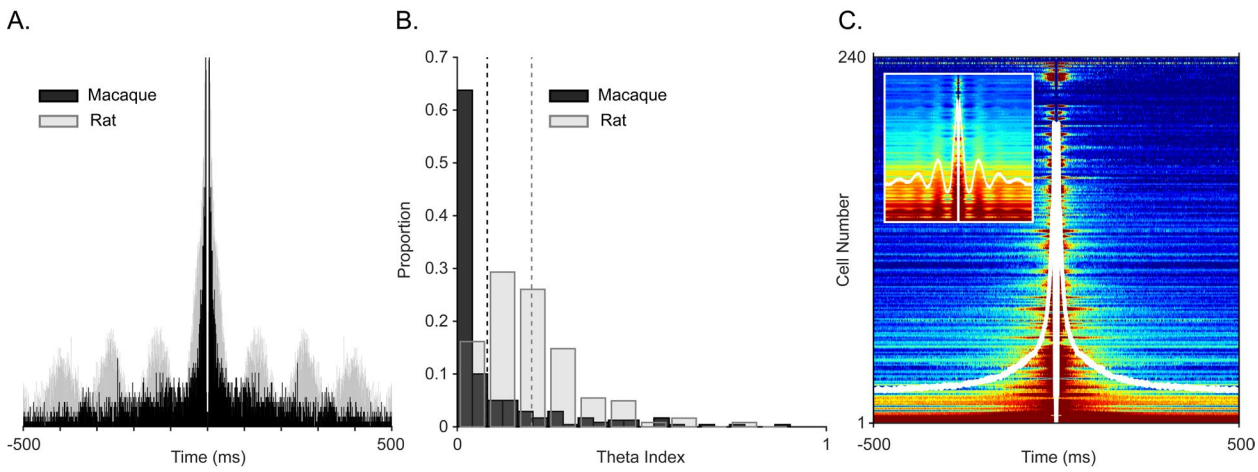

Figure 3. Examining spiking periodicity for theta modulation in macaque hippocampus. **A.** Autocorrelogram of an example "theta" unit from Figure 2A (black, N= 945 total spikes) and a theta-modulated unit in the rat (grey, N= 5655 total spikes). **B.** Distribution of the theta index in CA1 units from this study (black, N=240 units), and CA1 units of rat (gray, N=197 units). Dashed lines show mean values, color-coded by species. **C.** Sorted autocorrelograms of CA1 units, with mean, population ACG is shown as a white trace. Inset: same as the main plot but for rats.

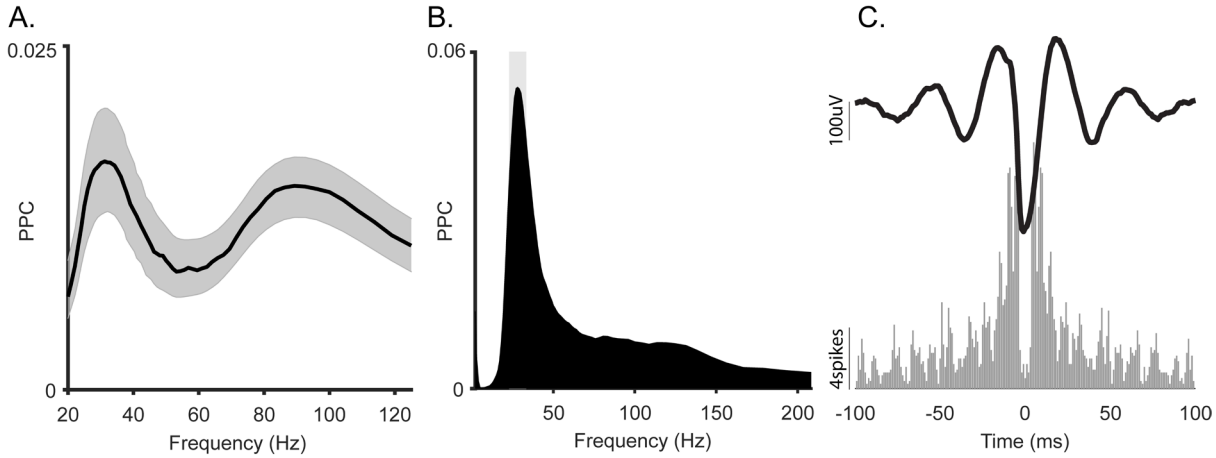

Figure 4. Spike-LFP coherence of the slow gamma oscillation in macaque hippocampus. **A.** Average spike-LFP coherence in gamma frequency range. Shading shows 95% bootstrap confidence interval. **B.** Spike-LFP coherence for a representative gamma-locked unit. This unit had a significant peak at 30Hz ($p<0.05$, permutation test and Rayleigh test $p<0.05$). **C. Top:** Spike-triggered average LFP of the unit in B. **Bottom**: Autocorrelogram of the same unit.

Discussion

In this study we evaluated the oscillatory dynamics of the primate hippocampus during two general behavioral states: first, during 'online' states of awake active behavior and second, during offline states. The waking-behavior recordings included stationary monkeys who were engaged in the memory-guided visual exploration, and freely-moving monkeys exploring their environment. The offline-state recordings included post-task quiescent states in the darkened booth, and the early stages of overnight sleep, respectively. The most prominent oscillation in amplitude and prevalence during alert active behavior was in the beta2 / slow gamma band (~20-35 Hz for stationary search and ~20-50Hz in freely-moving subjects). In contrast, theta-band (3-10 Hz, peak at ~8 Hz) amplitude and bout prevalence were greater during offline states of rest and sleep than during online active states. This bimodal oscillatory profile was also evident in finer temporal scales. Theta and beta2/gamma bands were decorrelated in the cross-frequency amplitude coupling, and in phase-amplitude bicoherence, quite unlike that observed in rodents (Zhou et al., 2019). Spike modulation by LFP frequency was seen in both bands; however, only the theta band effect appeared to be partially due to non-oscillatory field events, such as the sharp-wave ripple. Despite longer and more prevalent theta oscillations in rest, overall, we found no clear evidence of theta-periodic modulation. This contrasts with the strong and prevalent modulation seen using the same analysis methods applied to signal from the rat in homologous regions of CA1. Across several measures, we found consistent or compatible results in the coalescence among frequency bands, and between bands and

behavioral states within this study. These patterns differ from well-established spectral-behavioral coupling in rodents.

Dormant theta

In rat and mouse hippocampal LFPs, theta activity (centered at 6-9 Hz) is most consistently present during activated cortical states, i.e., during alert aroused behaviors and REM sleep(Buzsáki, 2002; Colgin, 2013; Nuñez and Buño, 2021; Vanderwolf, 1969). In contrast, theta gives way to sharp-wave ripples and irregular slow activity during quiescence and NREM sleep (Buzsáki, 2015, 1989). Further, theta 'nests' different frequencies of gamma in a phase-specific manner during these 'active' cortical states(Colgin and Moser, 2010; Colgin, 2016; Lasztóczi and Klausberger, 2014; Lisman and Jensen, 2013). And finally, most classes of cells in CA1 are modulated by the theta rhythm(Klausberger and Somogyi, 2008; Klausberger et al., 2003; Royer et al., 2010). Indeed, theta is so reliably present and so spectrally dominant in fields, spikes, and intracellular currents during the active states when gamma occurs, that studies of hippocampal gamma oscillations and spikes are commonly conditioned on them.

Monkey CA1 LFPs also show reliable, durable theta oscillations with peak frequencies at 6-9 Hz; however, where measured across states, they do not demonstrate the above characteristics of theta. Instead, they show divergent brain-behavior coupling to that seen in rodents. Much of the literature on humans and monkeys have focused on brief epochs of alert, goal-directed behaviors within stationary visual and visuospatial tasks and may therefore be suboptimal for detecting theta oscillations. Yet where rest or sleep have been measured, stronger, more durable theta field-potential oscillations appear during quiescence and NREM sleep (or anesthetized states (Kleen et al., 2021)) than during alert/task-on states or REM sleep (Bódizs et al., 2001; Cox et al., 2019; Moroni et al., 2007; Tamura et al., 2013; Uchida et al., 2001). Whereas these behavioral-state correlates of field potential oscillations apparently differ by species, local control of unit activity may nevertheless reveal strong underlying rhythmic motifs.

To better understand local modulation, we measured CA1 spiking activity as a function of the LFP oscillatory phase. All tested frequencies had at least some units that were preferentially phase locked to them, but the most common preferred frequencies were roughly matching the 3-10 Hz, 20-30 Hz, and 60-150 Hz bands. The lowest band would be consistent with theta modulation of local spiking, which has been reported using a few different methods in humans and macaques. Spike-field coherence in the theta frequency range was seen for microelectrode bundles including microwires in unspecified subregions of the human hippocampus (Rutishauser et al., 2010), and for recording sites estimated to be within the hippocampus proper of the freely-moving macaque (Mao et al., 2021), though in the latter

292 case, the higher gamma bands and delta bands were several times more likely to show SFC.
293 Within the theta band, spurious coherence may arise in response to nonrhythmic deflections
294 (Aru et al., 2015; de Cheveigné and Nelken, 2019; Jones, 2016; Vinck et al., 2022), such as
295 the slow components of the SWR which is especially prominent in macaques and human
296 (Hussin et al., 2020; Liu et al., 2022). Indeed, we found that SWRs (Figure 2-figure
297 supplement 1) disproportionally influenced the 2-10 Hz band (Figure 2B, D, E), whereas the
298 gamma frequency range was largely unaffected. Because SWRs occur infrequently, it was
299 somewhat surprising that SWR removal affected the overall results; however, the population
300 activity during ripples typically includes 2-10x firing rate increases in nearly all cell types
301 (Buzsáki, 2015; Hussin et al., 2020; Leonard et al., 2015; Skaggs et al., 2007). As such, each
302 ripple is likely contributing disproportionately to the spike-locked activity. In addition, we know
303 that visual (Katz et al., 2020; Rey et al., 2014; Roux et al., 2022) and saccade-elicited ('ERP-
304 like') responses in the hippocampus (Hoffman et al., 2013; Jutras et al., 2009; Katz et al., 2022)
305 increase theta-band power without necessarily producing harmonic oscillations. This would
306 presumably only affect the segments from search, not sleep. Future human and monkey
307 hippocampal studies should factor out the contributions of SWRs and to the same end
308 stimulus-locked transients, when evaluating low-frequency (<10 Hz) oscillations for non-
309 stationary signals and when using methods that do not discriminate oscillations from transient
310 deflections, as with spike-field coherence. The present results found residual coherence, and
311 in addition, the typical duration of sleep theta bouts would well exceed the SWR envelope, (as
312 shown in Video 1 and Figure 1-figure Supplement 4), therefore we consider the observed
313 spectral peaks during rest likely reflect true oscillations and not simply collections of evoked
314 transients.

315 The spike autocorrelogram is a more stringent measure of oscillatory modulation, not
316 susceptible to LFP spectral analysis artifacts. The <10 Hz range including the theta band failed
317 to show clear examples of theta modulation (Figure 2 supplement 2). This was not simply due
318 to low firing rates: even high firing rate cells, which should include 'theta-on' interneurons,
319 failed to show theta modulation. Indeed, the same analysis applied to units from a homologous
320 region of rat CA1 (Royer et al., 2010) showed a predominance of theta modulation (even after
321 pooling functional cell types). In light of our rest-related theta power and SWR-removed spike-
322 field coherence, this was somewhat surprising, but consistent with the results in free-flying
323 bats (Yartsev et al., 2011), monkeys (Courellis et al., 2019; Mao et al., 2021) and humans
324 (Qasim et al., 2021). In such cases, to observe spike timing regularity to field potentials, the
325 aperiodic – i.e. non oscillatory – slow fluctuations in the LFP must first be warped to 'fit' one
326 another, to create a pseudo-oscillation (Bush and Burgess, 2020; Eliav et al., 2018; Mao et
327 al., 2021; Qasim et al., 2021). Due to the different criteria used, compared to the theta-

rhythmic spiking reported in rodents, the theoretical or computational roles ascribed to the theta oscillations may need to be re-evaluated, or, more precisely defined in terms that do not depend on periodicity.

Slower oscillations, or irregular low-frequency components at 1-4 Hz 'delta' band, are more frequently correlated with spatial or associative memory effects (Goyal et al., 2020; Vivekananda et al., 2021; Watrous et al., 2013), leading to the supposition that rodent hippocampal theta is simply faster than in primates (Jacobs, 2014; Mao, 2022). If our present results were based on two distinct oscillations – the faster 'offline' theta and the slower 'online/memory' delta band – we would have predicted anti-correlations or segmentation in the power plots into sub-bands. We have yet to see such a segmentation, but we would stress that this remains a candidate for closer inspection. Finer task behaviors might help to uncover this possible alert-behavior correlate. Even if this proves to be the case, it will raise further questions about which bands become considered homologous across species. If 1-4 Hz is envisaged as relating to septal-cholinergic theta in rats, what is the equivalent of the classic 8-Hz theta band in rats? Compounding this problem is a separate 1-4 Hz oscillation that was observed in rat hippocampus (Jackson et al., 2014; Schultheiss et al., 2020). When trying to consider homology across species, the LFP signals are only proxies for the underlying circuit activity. Identifying the local circuit motif, including receptor-specific neuromodulation in primates (Stewart and Fox, 1991) may help differentiate among various low-frequency oscillations and their functional roles across species.

Decoupled gamma

Gamma oscillations in rat and mouse CA1 comprise a wide high-frequency band (initially 40 - 100 Hz but more recently 20 or 30 – 100 Hz) known for tight coupling within the theta oscillation (Bragin et al., 1995a; Buzsáki et al., 1983; Colgin and Moser, 2010; Colgin et al., 2009; Tort et al., 2008). In line with this coupling, gamma shares behavioral state correlates with theta: waking exploratory states and REM sleep. We found that the slower part of the gamma range (<~70 Hz) is decoupled from theta. Consistent with this finding, gamma power is seen as a relatively strong oscillation in monkeys and humans during REM sleep (Cantero et al., 2003; Takeuchi et al., 2015; Tamura et al., 2013; Uchida et al., 2001), as in rodents. Gamma oscillations, when measured, are often associated with hippocampal processing (e.g. memory-guided search (Leonard et al., 2015; Montefusco-Siegmund et al., 2017), and retrieval (Montefusco-Siegmund et al., 2017) or subsequent memory effects (Jutras et al., 2009) in monkeys, or spatial coding and memory in rodents. In addition, a band-limited 20-40 Hz oscillation is seen in rodent CA1 (and is synchronized with LEC (Igarashi et al., 2014)) during discrete item cueing or retrieval such as in olfactory associative place and sequence

learning (Allen et al., 2016; França et al., 2014; Lansink et al., 2016; Lopes-Dos-Santos et al., 2018), and when exploring novel environments (França et al., 2021; Trimper et al., 2017). This frequency band is associated with activation of the trisynaptic pathway (DG and CA3, (Colgin, 2016; Fernández-Ruiz et al., 2021; Hsiao et al., 2016; Rangel et al., 2015)), but is also seen in coherent oscillations between CA1 and LEC (Igarashi et al., 2014) implicating direct, temporoammonic pathways, thus the origin of the observed gamma oscillations in primates will be an important topic for future research.

Gamma and theta coupling

The results of the current study show that theta oscillations are not prominent during awake behavior and do not couple with gamma, and thus, are not a good candidate for structuring possible gamma sub-bands. Although most studies in humans focus on coupling via slower or faster bands outside this range, we note two exceptions that ostensibly find increases in hippocampal theta-gamma coupling associated with active processing in the theta band (Axmacher et al., 2010; Stangl et al., 2021) and a third that included 5-11 Hz, for which the low-frequency-granting signal may have included the alpha band (Roux et al., 2022). Both of the former studies use macro-electrode iEEG with >1 mm contacts and 3-10mm spacing between contacts, along with MR/CT coregistration, which are estimated to be in some regions of the hippocampus proper in only a subset of participants. Thus, any apparent discrepancies to the present findings may involve the inclusion of extra-hippocampal signals, though this would still be interesting to understand. Signal localization notwithstanding, the first study of working memory reported a 6-10 Hz medial temporal lobe theta phase that was coupled with gamma oscillations (Axmacher et al., 2010). Although modulation strength was not associated with performance, modulation width predicted reaction time. Pertinent to the state correlates of theta, they show that the intertrial interval - i.e. a potentially offline state - shared a strong modulation, similar to that seen during the memory epoch, except at the onset of the WM epoch, where intertrial coherence was strongest. In the second study, recording MTL iEEG in ambulating patients, theta power did not increase with movement speed (if anything, it nominally decreased), and search during movement was associated with weaker theta; however, when stationary, some theta modulation was seen and in addition, general theta-gamma coupling was reported between 6-10 Hz and high gamma during movement and 6-10 Hz and a slower gamma when stationary and observing others (Stangl et al., 2021). The effects of eye movement evoked responses on this theta were not reported but saccade-locked increases in reported theta power, thus, it remains unclear what effect saccadic responses may have had on the reported theta gamma coupling. In the third study, using microwires, the most applicable measures to our study produced generally consistent results, including decreased theta and increased gamma power associated with successful

associative memory, and no difference in low-frequency spike field coherence for locally measured fields and spikes (Roux et al., 2022). Here, unlike the first study(Axmacher et al., 2010), the modulation of gamma power by peak 5-11 Hz phase was greater with successful memory (hits vs. misses). This might suggest a theta or alpha oscillation is regulating gamma magnitude; however, the MI measure of phase-amplitude coupling does not require a strong or periodic phase-granting signal to cluster gamma (Tort et al., 2010). Future studies may help to disentangle the role of periodic theta in contrast to saccadic or other evoked response waves, in clustering active gamma oscillations during active behaviors. At present, we suggest that gamma oscillations – across species - can nevertheless work as a standalone rhythmic activity to select among inputs by virtue of laminar specificity, including the activity of other hippocampal fields (e.g. CA3-Dentate gyrus) or extrahippocampal areas (e.g. Entorhinal cortex).

Our findings offer a hypothesis-generating framework for future analysis in (human and non-human) primate hippocampal physiology. The present results suggest that theta oscillations were not prevalent during search in primates and did not consistently modulate single unit activity, but rather form the strongest oscillatory marker of offline or quiescent states. Instead, beta2/slow gamma oscillations constitute the chief, self-contained oscillation that arises during active exploration in the primate hippocampus and stands as the most likely oscillation for organizing local dynamics during exploration. Aside from understanding the nature of these cross-species differences, future work may focus on the better-conserved aspects of CA1 activity, including gamma synchrony during exploration, locking of spiking to exploratory movements, and aperiodic spike timing measures that don’t require autocoherent oscillations. Despite several surface differences in hippocampal-behavioral coupling across phylogenetic orders, the underlying neural-circuit activity giving rise to these oscillations may yet reveal fundamentally conserved mechanisms.

425 Methods

426 **Subjects and task**

427 Two adult female macaques (Macaca mulatta, 'M1, M2') were used in the main, visuospatial
428 search experiments whose results are shown in all figures except those of the control
429 task/recordings from Figure 1-figure supplements 3. Data from M1 and M2 have been reported
430 previously (Hussin et al., 2020; Leonard and Hoffman, 2017; Leonard et al., 2015). The
431 apparatus, training procedure, and task have been described previously (Leonard and
432 Hoffman, 2017; Leonard et al., 2015), and are summarized briefly here. During search,
433 animals performed a hippocampally-dependent visual target-detection task. In the task,
434 seated, head-fixed monkeys were placed in front of a monitor and were required to identify a
435 target object from nontargets in unique visual scenes presented on a monitor positioned in
436 front of them, and report their selection of scene-unique target objects by holding their gaze
437 on the target region for a prolonged (≥800 ms) duration. Target objects were defined as a
438 changing item in a natural scene image, where the original and changed images were
439 presented in alternation, each lasting 500 ms, with a brief grey screen (50 ms) shown between
440 image presentations. An inter-trial interval (ITI) of 2–20 s followed each trial. The daily
441 sessions began and ended with a period of at least 10 min when no stimulus was presented
442 within the darkened booth and animals could sleep or sit quietly ('rest'). All procedures
443 associated with this task were conducted with approval from the local ethics and animal care
444 authorities (Animal Care Committee, Canadian Council on Animal Care). Two adult female
445 monkeys (*Macaca mulatta*, 'M2' and 'M3') were used in a separate experiment to extend the
446 analysis to include freely-behaving conditions. The search epochs of M2 were observational
447 (identified post-hoc) and of M3 were experimentally controlled. M2 was placed in an enriched
448 environment where she could actively forage, play with toys (manipulanda), walk, climb, self-
449 groom, and groom another animal. Blind raters denoted the times of foraging, walking, and
450 exploratory 'search' behaviors. M3 was placed in a testing enclosure equipped with multiple
451 touchscreens around the periphery that presented spatially distributed arrays of objects. To
452 obtain fluid reward the monkey was required to locate and select (touch) designated objects
453 in a global spatial sequence across the enclosure, thereby requiring visual search, reaches,
454 and walking/climbing during a trial. For M3 search data analysis, we extracted the trial
455 sequence duration + 2 seconds beyond the first/last touches of the sequence which included
456 goal-directed walking but excluded the intertrial intervals containing reward consumption or
457 idle time prior to the animal's approach and trial initiation. For both M2 and M3, rest epochs
458 consisted of 40 minutes of recordings in the housing area during the start of the "night" cycle
459 of the room's automatic lighting system. A total of 18 sessions (M3: 15, M2: 3) were analyzed
460 for both task and rest epochs. All procedures for M3 were conducted in accordance with the

approved protocols and authorized procedures under the local animal care authorities (Institutional Animal Care and Use Committee).

Electrophysiological and movement recordings

For monkeys M1, and M2, indwelling bundles of moveable platinum/tungsten multicore tetrodes (96 μm outer diameter; Thomas Recordings) were implanted into the anterior half of the hippocampus and lowered into CA1. In M3 we recorded from an indwelling active multichannel probe on an adjustable microdrive ('Deep Array' probe, beta-test design, Diagnostic Biochips, Inc.). Recording sites were verified with postoperative CT co-registered to pre-operative MRI and using functional landmarks that changed with lowering depth, including the emergence of depth-specific sharp-wave ripples in a unit-dense layer, as described in the previous studies (Figure 1-figure supplement 1, Figure 2-figure supplement 1). Post-explant MRI verified the electrode locations in M1 (Leonard et al., 2015). For the current study, we detected channels within the pyramidal layer based on the strongest amplitude of ripples during SWRs and single unit activity and only used these channels for all analyses. LFPs were digitally sampled at 32 kHz using a Digital Lynx acquisition system (Neuralynx, Inc.) and filtered between 0.5 Hz and 2 kHz for M1 and M2. LFPs for M2 and M3 that were used for results shown in Figure 1-figure supplement 2 were sampled at 30kHz using the active headstage and recorded using a Cube/Freelynx wireless recording system (Neuralynx, Inc.) to SD card (for rest) or using wireless transmission to the Cheetah acquisition system (for the task). Single-unit activity was filtered between 600 Hz and 6 kHz, recording the waveform for 1 ms around a threshold-triggered spike event. Spike sorting was performed semi-automatically using KlustaKwik based on wave shape, principal components, energy, and peak/valley across channels. This was followed by manual curation of clusters in MClust (A.D. Redish). We used the 3D accelerometer in Freelynx data acquisition system to record the movement of freely-behaving animal subjects during active search and rest. Angular velocity (AV) traces were recorded at 3kHz and samples were synchronized with the neural recording. For movement detection, we first calculated the vector norm of the 3 AV axes using `vecnorm` function in MATLAB. Then we thresholded the vector norm to find periods of time when the animal was moving. The threshold was calculated based on the vector norm of AV recordings when Freelynx was placed statically on a flat surface. In addition to the accelerometer data, we used recorded videos to detect animal behavioral states (e.g. sleep).

495 **Sharp wave ripple detection**

496 Sharp wave ripple (SWR) detection was performed on the tetrode channels of M1 and M2 with
497 the most visibly apparent ripple activity using the previously described method (Leonard et al.,
498 2015). Raw LFPs recorded from the tetrode channel were filtered between 100-250 Hz. To
499 determine the SWR envelope, filtered LFPs were transformed into z-scores and rectified, and
500 subjected to a secondary band-pass filter between 1-20 Hz. Events with a minimum amplitude
501 exceeding 3 SDs above the mean with a minimum duration of 50 ms, beginning and ending
502 at 1 SD were designated as potential ripples. High-frequency energy is present for non-SWR
503 events such as EMG and other non-biological noise, though these artifacts are distinct from
504 ripples because the latter are restricted to the regions near the pyramidal layer. For artifact
505 (non-ripple-event) rejection, a distant tetrode channel was selected as a 'noise detecting'
506 channel (Talakoub et al., 2016). Events that were concurrently detected on the noise channel
507 and the 'ripple-layer' channel were removed from the ripple pool. High gamma (80-120Hz) and
508 high-frequency oscillations (HFO, 110-160Hz) events were similarly identified, but with the
509 filter criterion set at 80 –120 and 110 –160 Hz, respectively, and in both cases identifying
510 peaks as those > 1 SD. Duplicate High gamma/HFO and SWR events were labeled as SWRs.
511 Events with a repetition rate <125 ms were considered a single event.

512

513 **Power Spectral Parametrization and Fitting**

514 To compare the spectral content during search and rest, we selected successfully completed
515 trials lasting longer than 1 second. For the rest segments in M1 and M2, we extracted the LFP
516 signals that were recorded before the start of the task and after the end of the task when the
517 animal was in a dark environment in a quiescent or inactive state. For the rest segments in
518 M3, we extracted LFP signals recorded during the evening after the task, during the dark cycle
519 of the housing area. We used Welch's method with a 50%-overlapping 1024-sample sliding
520 Hanning window to estimate power spectra for the frequency range of 1 to 150 Hz with a
521 frequency resolution of 0.25 Hz.

522 To identify spectral peaks and compare between search and rest states, we parameterized
523 power spectra using the method described by Donoghue et al. (2020). This method models
524 power spectra as a combination of the 1/f frequency components (aperiodic) in addition to a
525 series of Gaussians that capture the presence of peaks (periodic components). The model
526 was fit to a frequency range between 1 to 200 Hz with a frequency resolution of 0.5 Hz.
527 Settings for the algorithm were set as: peak width limits: (0.5, 12); max number of
528 peaks: infinite; minimum peak height: 0; peak threshold: 2.0; and aperiodic mode: 'Fixed'.

To assess the statistical significance of the difference in parametrized spectra at each frequency, we used Wilcoxon signed rank test at $p < 0.05$ with FDR correction for multiple comparisons.

20-30 Hz sorted spectral density map:

We estimated the power spectral density using Welch's method described in the previous section to obtain (frequency * PSD segments) matrix. We then sorted the PSD segments based on the mean power in the 20-30 Hz frequency range and normalized each segment by dividing it by its median. We clustered all sorted segments into 50 total segments of equal size (frequency * 50 segments) by averaging original PSD sorted segments. We repeated this procedure across sessions and animals separately.

Cross-frequency Power Correlation

On continuous LFP time-series data, Welch's method with a 50%-overlapping 1024-sample sliding Hanning window was used to estimate the spectrogram for the frequency range of 1 to 150 Hz with a frequency resolution of 0.25 Hz.

We computed the pairwise correlation between cross-frequency power using the following formula (Masimore et al., 2004):

$$corr_{ij} = \frac{\sum_k (S_k(f_i) - \overline{S(f_i)})(S_k(f_j) - \overline{S(f_j)})}{\sigma_i \sigma_j}$$

where $S_k(f_i)$ is the PSD at the frequency f_i in time-window k, $\overline{S(f_i)}$ the averaged PSD at the frequency f_i overall sliding window, σ_i the standard deviation of the PSD at the frequency f_i, and k ranges over all sliding windows. In M3 this procedure was applied to the data segments extracted during task performance.

To test the null hypothesis that the power spectral time series of two different frequencies, f_i and f_j , are not coupled in the data, we performed a non-parametric surrogate data method with cluster-based multiple comparison correction (Thammasan and Miyakoshi, 2020). This method preserves the original data's statistical properties while generating time series that are randomized such that any possible nonlinear coupling is removed. In this method, we randomized time-window k differently for each frequency bin to build surrogate time-frequency time series' and computed the surrogate cross-frequency power correlation. This process was

repeated 5000 times to produce distributions for the dataset in which the null hypothesis holds. The original, non-permuted data are then compared to the surrogate distribution to obtain uncorrected p-values. The significance threshold was selected to be 0.05. For cluster-based multiple comparison correction, all samples were selected whose p-value was smaller than 0.05. Selected samples were then clustered in connected sets based on their adjacency and the cluster size was calculated. This procedure was performed 5000 times to produce the distribution of cluster sizes. If cluster sizes in the original correlation matrix were larger than the cluster threshold at 95-th quantile, they were reported as significant. We performed this statistical procedure at the level of single channels per animal. We consider as robust significance those areas that were significant for at least 80% of all samples.

Hilbert amplitude envelope correlation

We applied a 3rd order Butterworth filter at each frequency of the LFP with a 2Hz bandwidth. We then Hilbert transformed the bandpass-filtered LFP and estimated the continuous amplitude envelope. We computed the pairwise correlation between cross-frequency amplitude envelope using previously described correlation method.

Bicoherence

For Bicoherence, we used the HOSA toolbox. Bicoherence was estimated for frequencies f_1 (1 to 75 Hz) and f_2 (1 -150 Hz) in steps of 1 Hz according to the following formula (Bullock et al., 1997):

$$B(f_1, f_2) = \frac{|\langle F_t(f_1)F_t(f_2)F_t^*(f_1+f_2)\rangle_t|}{\langle |F_t(f_1)F_t(f_2)F_t^*(f_1+f_2)|\rangle_t}$$

Where $F_t(f)$ is the signal's time-frequency transformation at time t, $|\ \ |$ represents the absolute value, and $\langle\ \ \rangle$ is the average over time. We set the segment length to 1024 samples for this analysis.

Bicoherence has a higher spectral resolution for disentangling harmonic from the non-harmonic cross-frequency coupling. Additionally, bicoherence relaxes the artificial spectral constraints introduced by conventional PAC, corrects for its poor biases, and accounts for asymmetry in the rhythms (Giehl et al., 2021; Kovach et al., 2018; Sheremet et al., 2016).

Theoretically, the bispectrum is statistically zero for linear systems with mutually independent Fourier coefficients. For nonlinear systems, the bispectrum will exhibit peaks at triads (f_n, f_m, f_{n+m}) that are phase correlated, measuring the degree of three-wave coupling (Sheremet et al., 2016). In practice, however, bicoherence has a positive bias The background activity of LFP signals can be estimated by properties of red noise which can then be used for significance testing (Bédard and Destexhe, 2009; Torrence and Compo, 1998). To calculate the statistical significance of the local autobicoherence, we generated red noise with the same length of our original signals and computed Bicoherence for the red noise sample. We repeated this procedure 5000 times to obtain the null distribution. We then compared the original data to the null distribution to obtain uncorrected p-values, thresholded for significance at 0.05. We then performed cluster-based multiple comparison correction as described in the Cross-frequency Power Correlation section.

Detection and prevalence of transient oscillatory events

We used the BOSC algorithm (Caplan et al., 2001; Hughes et al., 2012) to detect transient bouts of heightened frequency-specific power using a joint amplitude and duration thresholding procedure. A specific concern we wished to address was that the 1-s windowed power spectral method may result in false negatives (i.e. missing brief theta epochs) therefore we set a maximally-permissive duration threshold of three cycles, and an amplitude threshold using 6th order wavelets passing the 95th percentile of model fit distributions. From these detected events, we computed the occupancy rate using the formula:

$$Occupancy\ rate\ (\%) = \frac{Total\ duration\ of\ detected\ events}{Duration\ of\ the\ original\ signal} \times 100$$

Occupancy rate is a measure of prevalence, showing the percentage of time spent in an oscillatory event of a specific frequency, also referred to as $P_{episode}(f)$.

BOSC algorithm provides a logical matrix of the form [number of frequencies * timepoint] where values are 1 when an event was detected and 0 otherwise. For bout duration distributions we summed values across frequency ranges of interest and then performed the logical operation larger than 1, thus in MATLAB it will be, where `detected` is the BOSC output:

```
thresholded = sum(detected(ThetaRange,:))>=1;
```

We found start (thresholded switches from 0 to 1) and stop (thresholded switches from 1 to 0) of events and removed events that were incomplete, only had a start or stop, and computed duration. We then fitted a kernel probability distribution to the duration values using `fitdist`

621 function in MATLAB. We used bandwidths of 50 and 10 for theta and gamma oscillations
622 respectively.

623

624 **Spike-Field Synchronization:**

625 To quantify spike-field synchronization, we used fieldtrip toolbox (MATLAB) to compute
626 pairwise phase consistency (PPC) which is unbiased by the number of spikes (Vinck et al.,
627 2010). Raw continuous recordings were resampled with a 1000 Hz sampling rate. The spectral
628 content was estimated with a frequency-dependent Hanning window with 5 cycles per
629 frequency and a frequency resolution of 1Hz. All detected spikes of a unit during the session
630 were included. To assess the statistical significance of spike-field synchronization, we first
631 used a non-parametric permutation test with minimal assumptions. In this procedure, the
632 distribution of PPC values was estimated from 1000 iterations of shuffled spike times of each
633 cell. We used the PPC distribution of shuffles to compute the PPC threshold for significance
634 at each frequency. We applied a threshold of uncorrected $p < 0.05$ to determine the significant
635 synchronization at each frequency. Only PPC values that exceeded the statistical threshold
636 and had a Rayleigh test $p<0.05$ and a minimum peak and peak prominence of 0.005 were
637 reported as significant. To obtain the probability distribution of observing significant PPC
638 values at a frequency, we fitted a kernel probability distribution to significant frequency values
639 using `fitdist` function in MATLAB. We used a bandwidth of 4.

640 To compare spike-field synchronization during SWRs, we extracted spikes inside a 600ms
641 window centered around the SWR events and computed PPC [PPC_{SWR}]. These spikes were
642 then excluded from the unit spike timestamps and PPC was calculated for the remaining
643 'residual' spikes [$PPC_{residual}$]. PPC_{SWR} was then compared with $PPC_{residual}$. Only cells with at
644 least 20 spikes during ripple time windows were included in this analysis.

645 To test the significance of differences in spike-field coupling within SWR epochs or excluding
646 them, on a per-unit basis, spikes were randomly selected and assigned to SWR and residual
647 conditions. In this random selection, spike counts were controlled to correspond to the original
648 condition. We performed the random selection 1000 times and measured the difference
649 between PPC in each iteration to obtain the null distribution. Then, we grouped frequencies
650 into 5 bands 2-3, 4-10, 11-20, 21-40, 41-100, 101-200 Hz. In each frequency band, we found
651 the peak frequency at which the absolute PPC difference was largest and only tested these
652 for significance. If the p-value of the PPC difference was less than 0.05 (two-tailed) after FDR
653 correction, it was labeled as significant.

Theta modulation index (TMI) Estimation

We used the method described by Royer et al. (2010) to quantify the degree of theta modulation in single units. For all units, we first computed the autocorrelogram of the cell, in 10 ms bins from -500 to +500 ms, normalized to the maximum value between 100 and 150 ms (corresponding to theta modulation), and clipped all values above 1. We only included autocorrelograms with at least 100 counts for further steps (N=240 units). We then fit each autocorrelogram with the following function:

$$y(t) = [a(sin(\omega t) + 1) + b] \ * \ \mathrm{e}^{-|t|/\tau_1} + c \ * \ \mathrm{e}^{-t^2/\tau_2^2}$$

Where t is the autocorrelogram time lag from -700 to 700ms, and $a - c$, ω, and τ_{1-2} were fit using the $fminsearch$ optimization function in MATLAB. The theta indexes were defined as the ratio of the fit parameters a/b. For best-fitting performance, we restricted possible values for ω to (4, 10), for a and b to non-negative values, for c to (0, 0.2), and for τ_2 to (0, 0.05).

Additional single unit datasets

To generate example plots of theta rhythmic cells (Figure 3), recordings from the Buzsáki laboratory were included (https://buzsakilab.nyumc.org/datasets/).

Acknowledgments

The authors wish to thank A. Maurer for thoughtful comments on the manuscript and W. Zinke and I. Hayes for technical support for the wireless recordings. This work was funded by the Krembil Foundation, Brain Canada, NSERC, the Whitehall Foundation, NEI P30EY008126, and NIH R01 NS127128.

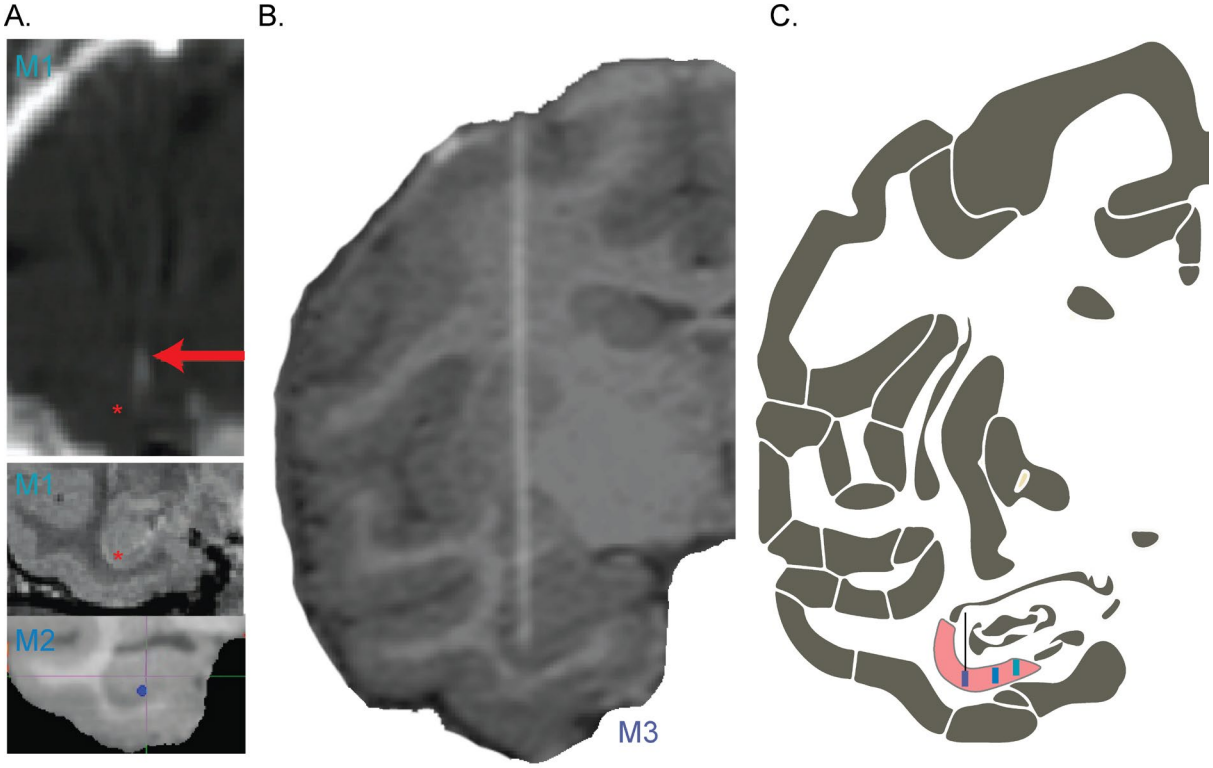

677

678 **Figure 1-figure supplement 1. Electrode Localization. A.** Coronal MR and CT images of hippocampal electrode trajectories.
679 CT image of implanted electrode bundle (top) shows the electrode tracts (white puff, red arrow) with deepest electrodes targeting
680 CA1 confirmed in post-explant MR and via functional localization to the pyramidal layer (middle, M1). Red asterisk shown laterally
681 displaced at the depth of probe tip, for visibility. Bottom shows the location of the electrode tip from the CT image placed in a
682 coronal plane of the coregistered MR image for M2. **B.** Coronal view of CT-MR coregistered image showing the location of the
683 electrode for M3. **C.** Schematic coronal slice showing the location of the CA1 subfield in the hippocampus (pink) with M1, M2,
684 and M3 probe locations from right to left, collapsing across the coronal slab for visualization. Features were adapted from Saleem
685 and Logothetis atlas (2012).

686

687

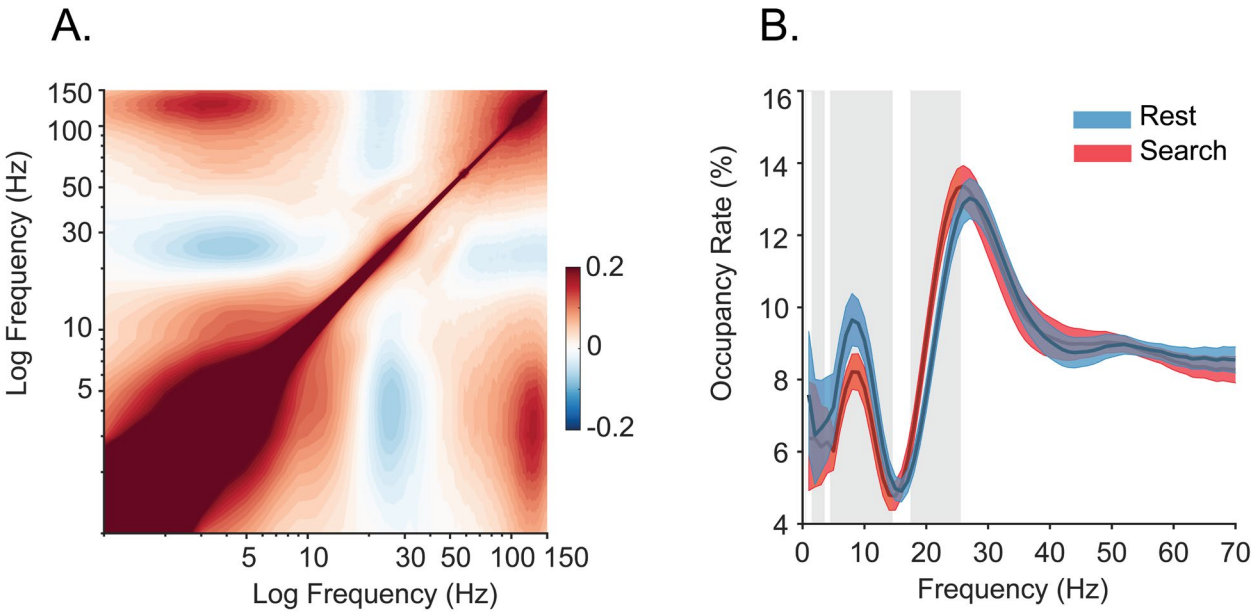

Figure 1-figure supplement 2. Spectral strength and coupling using alternate analysis methods. A. Cross-frequency pairwise correlation of Hilbert (amplitude) envelope (N = 42 sessions), which is sensitive to finer temporal coupling resolution than that of main Figure 1. Results are qualitatively indistinguishable. **B.** Prevalence of frequency-specific bouts during search (red), and rest (blue) with shaded 95% bootstrap confidence intervals (N = 42 sessions, $p<0.05$, Wilcoxon signed rank test, FDR corrected). Occupancy rate is the percent time spent in a detected bout of the specified frequency (also called 'Pepisode').

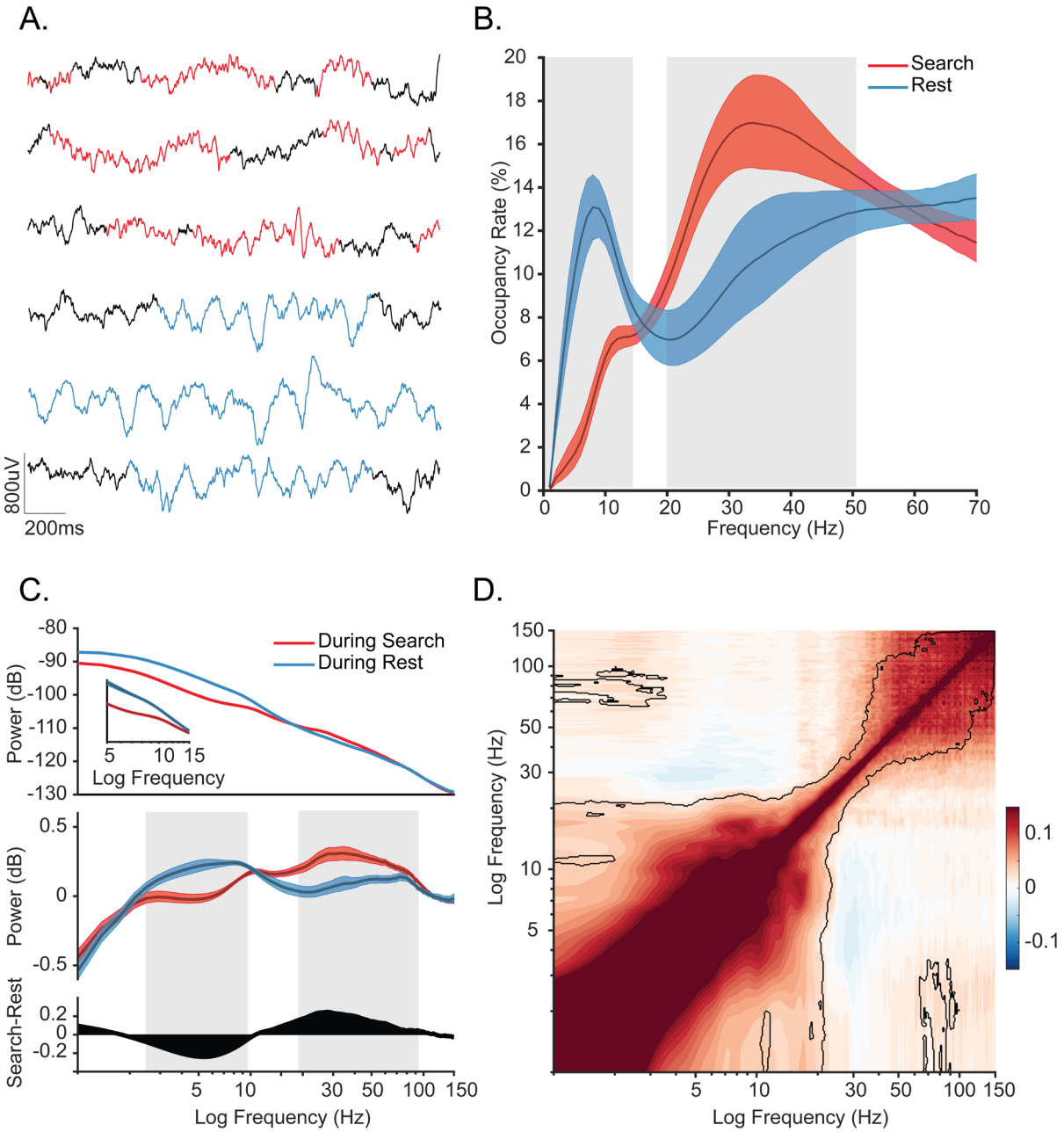

Figure 1-figure supplement 3. Oscillatory decoupling in CA1 of freely-behaving monkeys. A. Example detected oscillations in 4-8Hz and 25-40Hz frequency range during awake, free behavior (red), and sleep (blue) overlaid on wideband LFP in CA1 of a monkey (black). **B.** Prevalence of frequency-specific bouts during search (red), and rest (blue) with shaded 95% bootstrap confidence intervals (N = 18 sessions, p<0.05, Wilcoxon signed rank test, FDR corrected). **C.** ***Top.*** Mean power spectral density during search (red), and rest (blue). *Inset*: mean power for low frequencies of the main plot, with shaded 95% bootstrap confidence interval (N=18 sessions). ***Middle.*** Power spectral density after fitting and subtracting the aperiodic 1/f component during search and rest, with shaded 95% bootstrap confidence intervals. Gray areas show significant differences in power across behavioral epochs (p<0.05, Wilcoxon signed rank test, FDR corrected) ***Bottom.*** Power difference between search and rest. **D.** Average cross-frequency power comodulogram (N=18 sessions). Dark outline represents areas that were significant in at least 80% of samples (p < 0.05, cluster-based permutation test corrected for multiple comparisons).

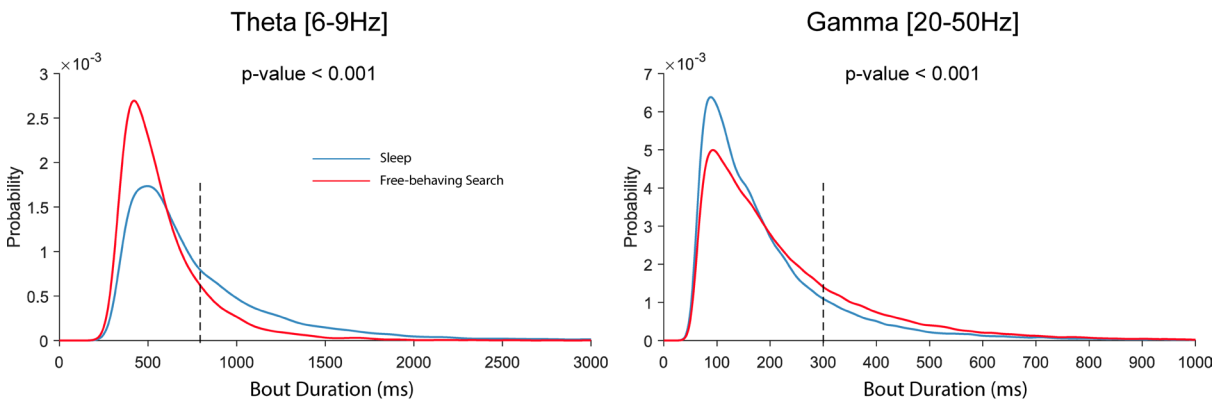

Figure 1-figure supplement 4. Probability distribution of bout durations. ***Left*** Distribution of detected bout durations for theta [6-9Hz] oscillation. Red, and blue show distribution for detected bouts during active search and offline behavioral states respectively (p<0.05, Wilcoxon signed-rank test). For reference, the black dotted line indicates 800ms, or approximately twice the duration of SWR low-frequency components (see **Figure 2-figure supplement 1**). ***Right*** same as the left plots but for gamma oscillations [20-50Hz]. The black dotted line indicates 300ms, indicating durations that would exceed two typical theta cycles. The lower end of the duration distribution is bounded by the duration threshold in the BOSC algorithm.

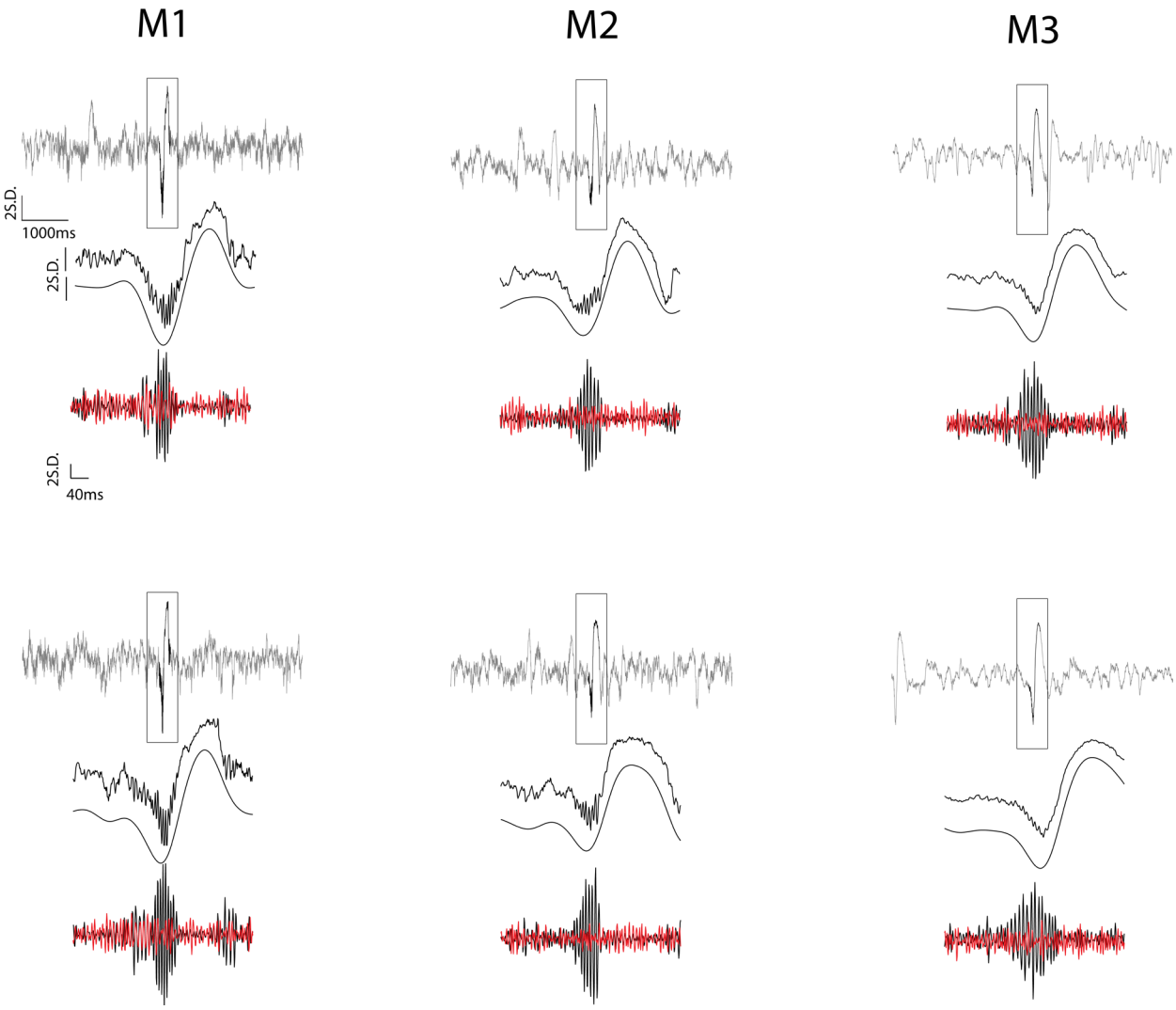

Figure 2-figure supplement 1. Examples of detected ripple events. For each example, the first row shows 6 seconds of z-normalized broadband signal centered at a ripple peak. Second row illustrates the zoomed-in (400ms) broadband LFP locked to ripple peak and narrow-band [<10Hz] trace of that example. Note the large amplitude deflection envelope accompanying ripples in the examples. These deflections possess similar power content as theta oscillations. Third row shows a bandpass [100-250Hz] filtered trace of the ripple (black) and of a simultaneously recorded signal from a hippocampal channel outside the layer (red), revealing the spatial localization of the ripples. The distant channels were used to remove high-frequency noise that can fall in the frequency spectrum of ripples but are apparent across channels due to volume conduction.

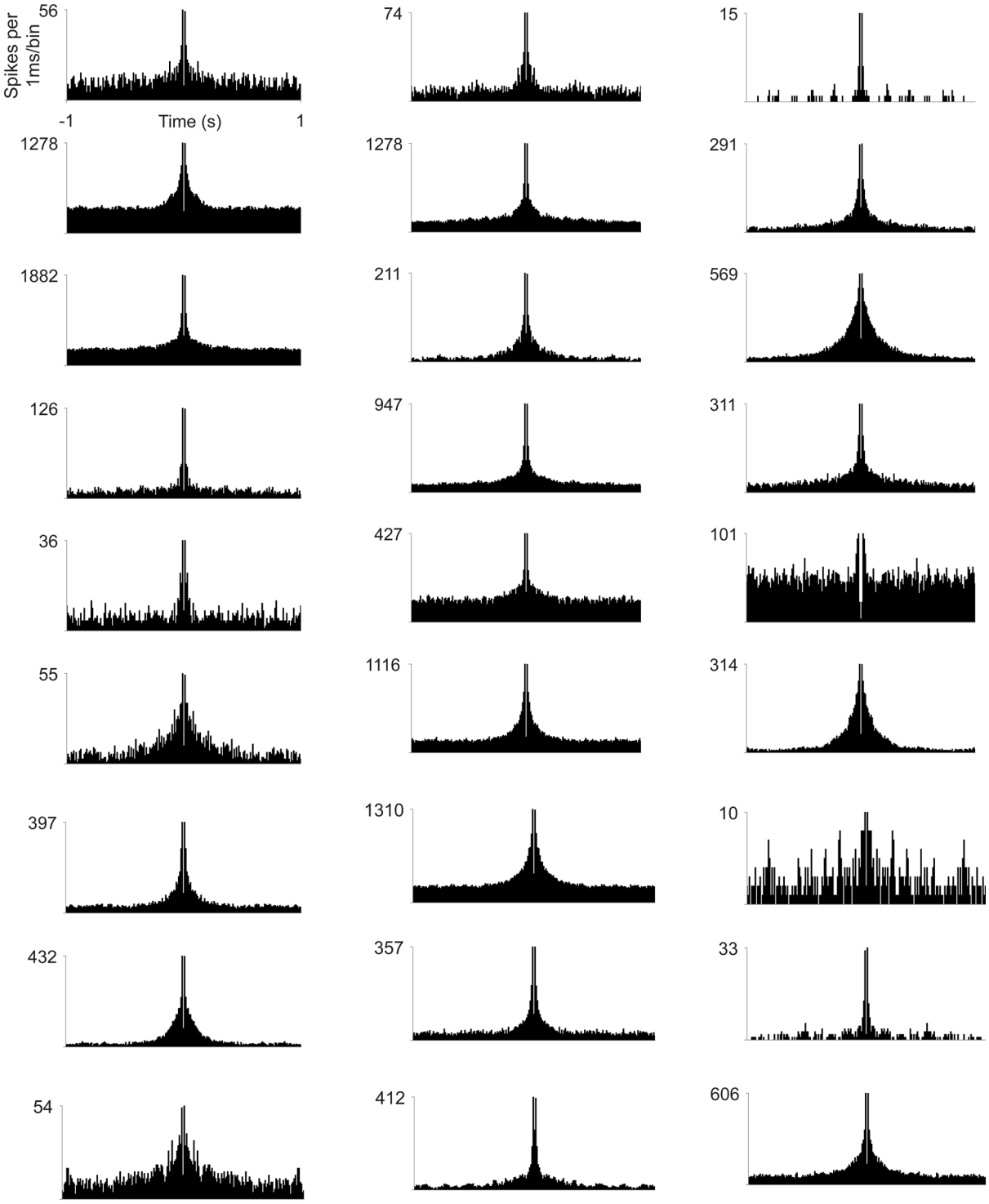

Figure 2-figure supplement 1. Spike-train autocorrelograms of example hippocampal cells. Note the absence of any clear temporal modulation in the theta range. Examples were selected to represent different baseline firing rates. Bin size, 1 ms.

Bibliography

Allen TA, Salz DM, McKenzie S, Fortin NJ. 2016. Nonspatial sequence coding in CA1 neurons. *J Neurosci* **36**:1547–1563. doi:10.1523/JNEUROSCI.2874-15.2016

Aru Juhan, Aru Jaan, Priesemann V, Wibral M, Lana L, Pipa G, Singer W, Vicente R. 2015. Untangling cross-frequency coupling in neuroscience. *Curr Opin Neurobiol* **31**:51–61. doi:10.1016/j.conb.2014.08.002

Axmacher N, Henseler MM, Jensen O, Weinreich I, Elger CE, Fell J. 2010. Cross-frequency coupling supports multi-item working memory in the human hippocampus. *Proc Natl Acad Sci USA* **107**:3228–3233. doi:10.1073/pnas.0911531107

Bédard C, Destexhe A. 2009. Macroscopic models of local field potentials and the apparent 1/f noise in brain activity. *Biophys J* **96**:2589–2603. doi:10.1016/j.bpj.2008.12.3951

Bódizs R, Kántor S, Szabó G, Szûcs A, Erõss L, Halász P. 2001. Rhythmic hippocampal slow oscillation characterizes REM sleep in humans. *Hippocampus* **11**:747–753. doi:10.1002/hipo.1090

Bragin A, Jandó G, Nádasdy Z, Hetke J, Wise K, Buzsáki G. 1995a. Gamma (40-100 Hz) oscillation in the hippocampus of the behaving rat. *J Neurosci* **15**:47–60. doi:10.1523/JNEUROSCI.15-01-00047.1995

Bragin A, Jandó G, Nádasdy Z, van Landeghem M, Buzsáki G. 1995b. Dentate EEG spikes and associated interneuronal population bursts in the hippocampal hilar region of the rat. *J Neurophysiol* **73**:1691–1705. doi:10.1152/jn.1995.73.4.1691

Bullock TH, Achimowicz JZ, Duckrow RB, Spencer SS, Iragui-Madoz VJ. 1997. Bicoherence of intracranial EEG in sleep, wakefulness and seizures. *Electroencephalogr Clin Neurophysiol* **103**:661–678. doi:10.1016/s0013-4694(97)00087-4

Bush D, Burgess N. 2020. Advantages and detection of phase coding in the absence of rhythmicity. *Hippocampus*. doi:10.1002/hipo.23199

Buzsáki G, Draguhn A. 2004. Neuronal oscillations in cortical networks. *Science* **304**:1926–1929. doi:10.1126/science.1099745

Buzsáki G, Leung LW, Vanderwolf CH. 1983. Cellular bases of hippocampal EEG in the behaving rat. *Brain Res* **287**:139–171. doi:10.1016/0165-0173(83)90037-1

Buzsáki G, Wang X-J. 2012. Mechanisms of gamma oscillations. *Annu Rev Neurosci* **35**:203–225. doi:10.1146/annurev-neuro-062111-150444

Buzsáki G. 2015. Hippocampal sharp wave-ripple: A cognitive biomarker for episodic memory and planning. *Hippocampus* **25**:1073–1188. doi:10.1002/hipo.22488

Buzsáki G. 2002. Theta oscillations in the hippocampus. *Neuron* **33**:325–340. doi:10.1016/S0896-6273(02)00586-X

Buzsáki G. 1996. The hippocampo-neocortical dialogue. *Cereb Cortex* **6**:81–92. doi:10.1093/cercor/6.2.81

Buzsáki G. 1989. Two-stage model of memory trace formation: a role for “noisy” brain states. *Neuroscience* **31**:551–570. doi:10.1016/0306-4522(89)90423-5

Cacucci F, Lever C, Wills TJ, Burgess N, O’Keefe J. 2004. Theta-modulated place-by-direction cells in the hippocampal formation in the rat. *J Neurosci* **24**:8265–8277. doi:10.1523/JNEUROSCI.2635-04.2004

Cantero JL, Atienza M, Stickgold R, Kahana MJ, Madsen JR, Kocsis B. 2003. Sleep-dependent theta oscillations in the human hippocampus and neocortex. *J Neurosci* **23**:10897–10903. doi:10.1523/JNEUROSCI.23-34-10897.2003

Caplan JB, Madsen JR, Raghavachari S, Kahana MJ. 2001. Distinct patterns of brain oscillations underlie two basic parameters of human maze learning. *J Neurophysiol* **86**:368–380. doi:10.1152/jn.2001.86.1.368

Colgin LL, Denninger T, Fyhn M, Hafting T, Bonnevie T, Jensen O, Moser M-B, Moser EI. 2009. Frequency of gamma oscillations routes flow of information in the hippocampus. *Nature* **462**:353–357. doi:10.1038/nature08573

Colgin LL, Moser EI. 2010. Gamma oscillations in the hippocampus. *Physiology (Bethesda)* **25**:319–329. doi:10.1152/physiol.00021.2010

Colgin LL. 2016. Rhythms of the hippocampal network. *Nat Rev Neurosci* **17**:239–249. doi:10.1038/nrn.2016.21

Colgin LL. 2013. Mechanisms and functions of theta rhythms. *Annu Rev Neurosci* **36**:295–312. doi:10.1146/annurev-neuro-062012-170330

Courellis HS, Nummela SU, Metke M, Diehl GW, Bussell R, Cauwenberghs G, Miller CT. 2019. Spatial encoding in primate hippocampus during free navigation. *PLoS Biol* **17**:e3000546. doi:10.1371/journal.pbio.3000546

Cox R, Rüber T, Staresina BP, Fell J. 2019. Heterogeneous profiles of coupled sleep oscillations in human hippocampus. *Neuroimage* **202**:116178. doi:10.1016/j.neuroimage.2019.116178

Csicsvari J, Jamieson B, Wise KD, Buzsáki G. 2003. Mechanisms of gamma oscillations in the hippocampus of the behaving rat. *Neuron* **37**:311–322. doi:10.1016/s0896-6273(02)01169-8

de Cheveigné A, Nelken I. 2019. Filters: when, why, and how (not) to use them. *Neuron* **102**:280–293. doi:10.1016/j.neuron.2019.02.039

Demanuele C, James CJ, Sonuga-Barke EJ. 2007. Distinguishing low frequency oscillations within the 1/f spectral behaviour of electromagnetic brain signals. *Behav Brain Funct* **3**:62. doi:10.1186/1744-9081-3-62

Donoghue T, Haller M, Peterson EJ, Varma P, Sebastian P, Gao R, Noto T, Lara AH, Wallis JD, Knight RT, Shestyuk A, Voytek B. 2020. Parameterizing neural power spectra into periodic and aperiodic components. *Nat Neurosci* **23**:1655–1665. doi:10.1038/s41593-020-00744-x

Eliav T, Geva-Sagiv M, Yartsev MM, Finkelstein A, Rubin A, Las L, Ulanovsky N. 2018. Nonoscillatory phase coding and synchronization in the bat hippocampal formation. *Cell* **175**:1119-1130.e15. doi:10.1016/j.cell.2018.09.017

Fernández-Ruiz A, Oliva A, Soula M, Rocha-Almeida F, Nagy GA, Martin-Vazquez G, Buzsáki G. 2021. Gamma rhythm communication between entorhinal cortex and dentate gyrus neuronal assemblies. *Science* **372**. doi:10.1126/science.abf3119

França ASC, Borgesius NZ, Souza BC, Cohen MX. 2021. Beta2 Oscillations in Hippocampal-Cortical Circuits During Novelty Detection. *Front Syst Neurosci* **15**:617388. doi:10.3389/fnsys.2021.617388

França ASC, do Nascimento GC, Lopes-dos-Santos V, Muratori L, Ribeiro S, Lobão-Soares B, Tort ABL. 2014. Beta2 oscillations (23-30 Hz) in the mouse hippocampus during novel object recognition. *Eur J Neurosci* **40**:3693–3703. doi:10.1111/ejn.12739

Fuhrmann F, Justus D, Sosulina L, Kaneko H, Beutel T, Friedrichs D, Schoch S, Schwarz MK, Fuhrmann M, Remy S. 2015. Locomotion, Theta Oscillations, and the Speed-Correlated Firing of Hippocampal Neurons Are Controlled by a Medial Septal Glutamatergic Circuit. *Neuron* **86**:1253–1264. doi:10.1016/j.neuron.2015.05.001

Giehl J, Noury N, Siegel M. 2021. Dissociating harmonic and non-harmonic phase-amplitude coupling in the human brain. *Neuroimage* **227**:117648. doi:10.1016/j.neuroimage.2020.117648

Goyal A, Miller J, Qasim SE, Watrous AJ, Zhang H, Stein JM, Inman CS, Gross RE, Willie JT, Lega B, Lin J-J, Sharan A, Wu C, Sperling MR, Sheth SA, McKhann GM, Smith EH, Schevon C, Jacobs J. 2020. Functionally distinct high and low theta oscillations in the human hippocampus. *Nat Commun* **11**:2469. doi:10.1038/s41467-020-15670-6

Green JD, Arduini AA. 1954. Hippocampal electrical activity in arousal. *J Neurophysiol* **17**:533–557. doi:10.1152/jn.1954.17.6.533

Hahn G, Ponce-Alvarez A, Deco G, Aertsen A, Kumar A. 2019. Portraits of communication in neuronal networks. *Nat Rev Neurosci* **20**:117–127. doi:10.1038/s41583-018-0094-0

Halgren E, Babb TL, Crandall PH. 1978. Human hippocampal formation EEG desynchronizes during attentiveness and movement. *Electroencephalogr Clin Neurophysiol* **44**:778–781. doi:10.1016/0013-4694(78)90212-2

Herweg NA, Solomon EA, Kahana MJ. 2020. Theta oscillations in human memory. *Trends Cogn Sci (Regul Ed)* **24**:208–227. doi:10.1016/j.tics.2019.12.006

Hoffman KL, Dragan MC, Leonard TK, Micheli C, Montefusco-Siegmund R, Valiante TA. 2013. Saccades during visual exploration align hippocampal 3-8 Hz rhythms in human and non-human primates. *Front Syst Neurosci* **7**:43. doi:10.3389/fnsys.2013.00043

Hsiao Y-T, Zheng C, Colgin LL. 2016. Slow gamma rhythms in CA3 are entrained by slow gamma activity in the dentate gyrus. *J Neurophysiol* **116**:2594–2603. doi:10.1152/jn.00499.2016

Hughes AM, Whitten TA, Caplan JB, Dickson CT. 2012. BOSC: a better oscillation detection method, extracts both sustained and transient rhythms from rat hippocampal recordings. *Hippocampus* **22**:1417–1428. doi:10.1002/hipo.20979

Hussin AT, Leonard TK, Hoffman KL. 2020. Sharp-wave ripple features in macaques depend on behavioral state and cell-type specific firing. *Hippocampus* **30**:50–59. doi:10.1002/hipo.23046

Hyafil A. 2015. Misidentifications of specific forms of cross-frequency coupling: three warnings. *Front Neurosci* **9**:370. doi:10.3389/fnins.2015.00370

Igarashi KM, Lu L, Colgin LL, Moser M-B, Moser EI. 2014. Coordination of entorhinal-hippocampal ensemble activity during associative learning. *Nature* **510**:143–147. doi:10.1038/nature13162

Jackson J, Amilhon B, Goutagny R, Bott J-B, Manseau F, Kortleven C, Bressler SL, Williams S. 2014. Reversal of theta rhythm flow through intact hippocampal circuits. *Nat Neurosci* **17**:1362–1370. doi:10.1038/nn.3803

Jacobs J. 2014. Hippocampal theta oscillations are slower in humans than in rodents: implications for models of spatial navigation and memory. *Philos Trans R Soc Lond B Biol Sci* **369**:20130304. doi:10.1098/rstb.2013.0304

Jones SR. 2016. When brain rhythms aren't "rhythmic": implication for their mechanisms and meaning. *Curr Opin Neurobiol* **40**:72–80. doi:10.1016/j.conb.2016.06.010

Jutras MJ, Fries P, Buffalo EA. 2013. Oscillatory activity in the monkey hippocampus during visual exploration and memory formation. *Proc Natl Acad Sci USA* **110**:13144–13149. doi:10.1073/pnas.1302351110

Jutras MJ, Fries P, Buffalo EA. 2009. Gamma-band synchronization in the macaque hippocampus and memory formation. *J Neurosci* **29**:12521–12531. doi:10.1523/JNEUROSCI.0640-09.2009

Katz CN, Patel K, Talakoub O, Groppe D, Hoffman K, Valiante TA. 2020. Differential Generation of Saccade, Fixation, and Image-Onset Event-Related Potentials in the Human Mesial Temporal Lobe. *Cereb Cortex* **30**:5502–5516. doi:10.1093/cercor/bhaa132

Katz CN, Schjetnan AGP, Patel K, Barkley V, Hoffman KL, Kalia SK, Duncan KD, Valiante TA. 2022. A corollary discharge mediates saccade-related inhibition of single units in mnemonic structures of the human brain. *Curr Biol* **32**:3082-3094.e4. doi:10.1016/j.cub.2022.06.015

Klausberger T, Magill PJ, Márton LF, Roberts JDB, Cobden PM, Buzsáki G, Somogyi P. 2003. Brain-state- and cell-type-specific firing of hippocampal interneurons in vivo. *Nature* **421**:844–848. doi:10.1038/nature01374

Klausberger T, Somogyi P. 2008. Neuronal diversity and temporal dynamics: the unity of hippocampal circuit operations. *Science* **321**:53–57. doi:10.1126/science.1149381

Kleen JK, Chung JE, Sellers KK, Zhou J, Triplett M, Lee K, Tooker A, Haque R, Chang EF. 2021. Bidirectional propagation of low frequency oscillations over the human hippocampal surface. *Nat Commun* **12**:2764. doi:10.1038/s41467-021-22850-5

Kovach CK, Oya H, Kawasaki H. 2018. The bispectrum and its relationship to phase-amplitude coupling. *Neuroimage* **173**:518–539. doi:10.1016/j.neuroimage.2018.02.033

Kramis R, Vanderwolf CH, Bland BH. 1975. Two types of hippocampal rhythmical slow activity in both the rabbit and the rat: relations to behavior and effects of atropine, diethyl ether, urethane, and pentobarbital. *Exp Neurol* **49**:58–85. doi:10.1016/0014-4886(75)90195-8

Lansink CS, Meijer GT, Lankelma JV, Vinck MA, Jackson JC, Pennartz CMA. 2016. Reward Expectancy Strengthens CA1 Theta and Beta Band Synchronization and Hippocampal-Ventral Striatal Coupling. *J Neurosci* **36**:10598–10610. doi:10.1523/JNEUROSCI.0682-16.2016

Lasztóczi B, Klausberger T. 2014. Layer-specific GABAergic control of distinct gamma oscillations in the CA1 hippocampus. *Neuron* **81**:1126–1139. doi:10.1016/j.neuron.2014.01.021

Leonard TK, Hoffman KL. 2017. Sharp-Wave Ripples in Primates Are Enhanced near Remembered Visual Objects. *Curr Biol* **27**:257–262. doi:10.1016/j.cub.2016.11.027

Leonard TK, Mikkila JM, Eskandar EN, Gerrard JL, Kaping D, Patel SR, Womelsdorf T, Hoffman KL. 2015. Sharp Wave Ripples during Visual Exploration in the Primate Hippocampus. *J Neurosci* **35**:14771–14782. doi:10.1523/JNEUROSCI.0864-15.2015

Lisman JE, Jensen O. 2013. The θ-γ neural code. *Neuron* **77**:1002–1016. doi:10.1016/j.neuron.2013.03.007

Liu AA, Henin S, Abbaspoor S, Bragin A, Buffalo EA, Farrell JS, Foster DJ, Frank LM, Gedankien T, Gotman J, Guidera JA, Hoffman KL, Jacobs J, Kahana MJ, Li L, Liao Z, Lin JJ, Losonczy A, Malach R, van der Meer MA, McClain K, McNaughton BL, Norman Y, Navas-Olive A, de la Prida LM, Rueckemann JW, Sakon JJ, Skelin I, Soltesz I, Staresina BP, Weiss SA, Wilson MA, Zaghloul KA, Zugaro M, Buzsáki G. 2022. A consensus statement on detection of hippocampal sharp wave ripples and differentiation from other fast oscillations. *Nat Commun* **13**:6000. doi:10.1038/s41467-022-33536-x

Lopes-Dos-Santos V, van de Ven GM, Morley A, Trouche S, Campo-Urriza N, Dupret D. 2018. Parsing Hippocampal Theta Oscillations by Nested Spectral Components during Spatial Exploration and Memory-Guided Behavior. *Neuron* **100**:940-952.e7. doi:10.1016/j.neuron.2018.09.031

Maier N, Nimmrich V, Draguhn A. 2003. Cellular and network mechanisms underlying spontaneous sharp wave-ripple complexes in mouse hippocampal slices. *J Physiol (Lond)* **550**:873–887. doi:10.1113/jphysiol.2003.044602

Mao D, Avila E, Caziot B, Laurens J, Dickman JD, Angelaki DE. 2021. Spatial modulation of hippocampal activity in freely moving macaques. *Neuron* **109**:3521-3534.e6. doi:10.1016/j.neuron.2021.09.032

Mao D. 2022. Neural correlates of spatial navigation in primate hippocampus. *Neurosci Bull*. doi:10.1007/s12264-022-00968-w

Masimore B, Kakalios J, Redish AD. 2004. Measuring fundamental frequencies in local field potentials. *J Neurosci Methods* **138**:97–105. doi:10.1016/j.jneumeth.2004.03.014

McFarland WL, Teitelbaum H, Hedges EK. 1975. Relationship between hippocampal theta activity and running speed in the rat. *J Comp Physiol Psychol* **88**:324–328. doi:10.1037/h0076177

Montefusco-Siegmund R, Leonard TK, Hoffman KL. 2017. Hippocampal gamma-band Synchrony and pupillary responses index memory during visual search. *Hippocampus* **27**:425–434. doi:10.1002/hipo.22702

Moroni F, Nobili L, Curcio G, De Carli F, Fratello F, Marzano C, De Gennaro L, Ferrillo F, Cossu M, Francione S, Lo Russo G, Bertini M, Ferrara M. 2007. Sleep in the human hippocampus: a stereo-EEG study. *PLoS ONE* **2**:e867. doi:10.1371/journal.pone.0000867

M Aghajan Z, Schuette P, Fields TA, Tran ME, Siddiqui SM, Hasulak NR, Tcheng TK, Eliashiv D, Mankin EA, Stern J, Fried I, Suthana N. 2017. Theta Oscillations in the Human Medial Temporal Lobe during Real-World Ambulatory Movement. *Curr Biol* **27**:3743-3751.e3. doi:10.1016/j.cub.2017.10.062

Nuñez A, Buño W. 2021. The theta rhythm of the hippocampus: from neuronal and circuit mechanisms to behavior. *Front Cell Neurosci* **15**:649262. doi:10.3389/fncel.2021.649262

O'Keefe J, Recce ML. 1993. Phase relationship between hippocampal place units and the EEG theta rhythm. *Hippocampus* **3**:317–330. doi:10.1002/hipo.450030307

Qasim SE, Fried I, Jacobs J. 2021. Phase precession in the human hippocampus and entorhinal cortex. *Cell* **184**:3242-3255.e10. doi:10.1016/j.cell.2021.04.017

Rangel LM, Chiba AA, Quinn LK. 2015. Theta and beta oscillatory dynamics in the dentate gyrus reveal a shift in network processing state during cue encounters. *Front Syst Neurosci* **9**:96. doi:10.3389/fnsys.2015.00096

Rex CS, Colgin LL, Jia Y, Casale M, Yanagihara TK, Debenedetti M, Gall CM, Kramar EA, Lynch G. 2009. Origins of an intrinsic hippocampal EEG pattern. *PLoS ONE* **4**:e7761. doi:10.1371/journal.pone.0007761

Rey HG, Fried I, Quian Quiroga R. 2014. Timing of single-neuron and local field potential responses in the human medial temporal lobe. *Curr Biol* **24**:299–304. doi:10.1016/j.cub.2013.12.004

Roux F, Parish G, Chelvarajah R, Rollings DT, Sawlani V, Hamer H, Gollwitzer S, Kreiselmeyer G, Ter Wal MJ, Kolibius L, Staresina BP, Wimber M, Self MW, Hanslmayr S. 2022. Oscillations support short latency co-firing of neurons during human episodic memory formation. *eLife* **11**. doi:10.7554/eLife.78109

Royer S, Sirota A, Patel J, Buzsáki G. 2010. Distinct representations and theta dynamics in dorsal and ventral hippocampus. *J Neurosci* **30**:1777–1787. doi:10.1523/JNEUROSCI.4681-09.2010

Rutishauser U, Ross IB, Mamelak AN, Schuman EM. 2010. Human memory strength is predicted by theta-frequency phase-locking of single neurons. *Nature* **464**:903–907. doi:10.1038/nature08860

Sainsbury RS. 1998. Hippocampal theta: a sensory-inhibition theory of function. *Neurosci Biobehav Rev* **22**:237–241. doi:10.1016/s0149-7634(97)00011-0

Schultheiss NW, Schlecht M, Jayachandran M, Brooks DR, McGlothan JL, Guilarte TR, Allen TA. 2020. Awake delta and theta-rhythmic hippocampal network modes during intermittent locomotor behaviors in the rat. *Behav Neurosci* **134**:529–546. doi:10.1037/bne0000409

Sheremet A, Burke SN, Maurer AP. 2016. Movement enhances the nonlinearity of hippocampal theta. *J Neurosci* **36**:4218–4230. doi:10.1523/JNEUROSCI.3564-15.2016

Skaggs WE, McNaughton BL, Permenter M, Archibeque M, Vogt J, Amaral DG, Barnes CA. 2007. EEG sharp waves and sparse ensemble unit activity in the macaque hippocampus. *J Neurophysiol* **98**:898–910. doi:10.1152/jn.00401.2007

Stangl M, Topalovic U, Inman CS, Hiller S, Villaroman D, Aghajan ZM, Christov-Moore L, Hasulak NR, Rao VR, Halpern CH, Eliashiv D, Fried I, Suthana N. 2021. Boundary-anchored neural mechanisms of location-encoding for self and others. *Nature* **589**:420–425. doi:10.1038/s41586-020-03073-y

Stewart M, Fox SE. 1991. Hippocampal theta activity in monkeys. *Brain Res* **538**:59–63. doi:10.1016/0006-8993(91)90376-7

Tai SK, Ma J, Ossenkopp K-P, Leung LS. 2012. Activation of immobility-related hippocampal theta by cholinergic septohippocampal neurons during vestibular stimulation. *Hippocampus* **22**:914–925. doi:10.1002/hipo.20955

Takeuchi S, Mima T, Murai R, Shimazu H, Isomura Y, Tsujimoto T. 2015. Gamma Oscillations and Their Cross-frequency Coupling in the Primate Hippocampus during Sleep. *Sleep* **38**:1085–1091. doi:10.5665/sleep.4818

Talakoub O, Gomez Palacio Schjetnan A, Valiante TA, Popovic MR, Hoffman KL. 2016. Closed-Loop Interruption of Hippocampal Ripples through Fornix Stimulation in the Non-Human Primate. *Brain Stimulat* **9**:911–918. doi:10.1016/j.brs.2016.07.010

Talakoub O, Sayegh PF, Womelsdorf T, Zinke W, Fries P, Lewis CM, Hoffman KL. 2019. Hippocampal and neocortical oscillations are tuned to behavioral state in freely-behaving macaques. *BioRxiv*. doi:10.1101/552877

Tamura R, Nishida H, Eifuku S, Fushiki H, Watanabe Y, Uchiyama K. 2013. Sleep-stage correlates of hippocampal electroencephalogram in primates. *PLoS ONE* **8**:e82994. doi:10.1371/journal.pone.0082994

Thammasan N, Miyakoshi M. 2020. Cross-Frequency Power-Power Coupling Analysis: A Useful Cross-Frequency Measure to Classify ICA-Decomposed EEG. *Sensors* **20**. doi:10.3390/s20247040

Torrence C, Compo GP. 1998. A practical guide to wavelet analysis. *Bull Amer Meteor Soc* **79**:61–78. doi:10.1175/1520-0477(1998)079<0061:APGTWA>2.0.CO;2

Tort ABL, Komorowski R, Eichenbaum H, Kopell N. 2010. Measuring phase-amplitude coupling between neuronal oscillations of different frequencies. *J Neurophysiol* **104**:1195–1210. doi:10.1152/jn.00106.2010

Tort ABL, Kramer MA, Thorn C, Gibson DJ, Kubota Y, Graybiel AM, Kopell NJ. 2008. Dynamic cross-frequency couplings of local field potential oscillations in rat striatum and hippocampus during performance of a T-maze task. *Proc Natl Acad Sci USA* **105**:20517–20522. doi:10.1073/pnas.0810524105

Trimper JB, Galloway CR, Jones AC, Mandi K, Manns JR. 2017. Gamma oscillations in rat hippocampal subregions dentate gyrus, CA3, CA1, and subiculum underlie associative memory encoding. *Cell Rep* **21**:2419–2432. doi:10.1016/j.celrep.2017.10.123

Uchida S, Maehara T, Hirai N, Okubo Y, Shimizu H. 2001. Cortical oscillations in human medial temporal lobe during wakefulness and all-night sleep. *Brain Res* **891**:7–19. doi:10.1016/s0006-8993(00)03154-1

Ulanovsky N, Moss CF. 2007. Hippocampal cellular and network activity in freely moving echolocating bats. *Nat Neurosci* **10**:224–233. doi:10.1038/nn1829

Vanderwolf CH. 1969. Hippocampal electrical activity and voluntary movement in the rat. *Electroencephalogr Clin Neurophysiol* **26**:407–418. doi:10.1016/0013-4694(69)90092-3

Vinck M, Uran C, Schneider M. 2022. Aperiodic processes explaining rhythms in behavior: A matter of false detection or definition? doi:10.31234/osf.io/wzvfh

Vinck M, van Wingerden M, Womelsdorf T, Fries P, Pennartz CMA. 2010. The pairwise phase consistency: a bias-free measure of rhythmic neuronal synchronization. *Neuroimage* **51**:112–122. doi:10.1016/j.neuroimage.2010.01.073

Vivekananda U, Bush D, Bisby JA, Baxendale S, Rodionov R, Diehl B, Chowdhury FA, McEvoy AW, Miserocchi A, Walker MC, Burgess N. 2021. Theta power and theta-gamma coupling support long-term spatial memory retrieval. *Hippocampus* **31**:213–220. doi:10.1002/hipo.23284

Watrous AJ, Lee DJ, Izadi A, Gurkoff GG, Shahlaie K, Ekstrom AD. 2013. A comparative study of human and rat hippocampal low-frequency oscillations during spatial navigation. *Hippocampus* **23**:656–661. doi:10.1002/hipo.22124

Whishaw IQ, Vanderwolf CH. 1973. Hippocampal EEG and behavior: changes in amplitude and frequency of RSA (theta rhythm) associated with spontaneous and learned movement patterns in rats and cats. *Behav Biol* **8**:461–484. doi:10.1016/S0091-6773(73)80041-0

Yartsev MM, Witter MP, Ulanovsky N. 2011. Grid cells without theta oscillations in the entorhinal cortex of bats. *Nature* **479**:103–107. doi:10.1038/nature10583

Ylinen A, Bragin A, Nádasdy Z, Jandó G, Szabó I, Sik A, Buzsáki G. 1995. Sharp wave-associated high-frequency oscillation (200 Hz) in the intact hippocampus: network and intracellular mechanisms. *J Neurosci* **15**:30–46.

Zhou Y, Sheremet A, Qin Y, Kennedy JP, DiCola NM, Burke SN, Maurer AP. 2019. Methodological considerations on the use of different spectral decomposition algorithms to study hippocampal rhythms. *eNeuro* **6**. doi:10.1523/ENEURO.0142-19.2019